



Spectroscopic Evolution in Ice Analogs of Trans-Neptunian Objects Exposed to Ionizing Radiation. I. Visible Reflectance Spectra and Colors

Chaojiang Zhang^{1,2} , Jia Wang^{1,2} , Andrew M. Turner^{1,2}, Leslie A. Young³ , and Ralf I. Kaiser^{1,2}

¹ Department of Chemistry, University of Hawaii at Mānoa, Honolulu, HI 96822, USA; ralfk@hawaii.edu

² W. M. Keck Laboratory in Astrochemistry, University of Hawaii at Mānoa, Honolulu, HI 96822, USA

³ Department of Space Studies, Southwest Research Institute, Boulder, CO 80302, USA; layoung@boulder.swri.edu

Received 2024 September 11; revised 2025 March 18; accepted 2025 March 27; published 2025 May 7

Abstract

Trans-Neptunian objects (TNOs) exhibit a color diversity containing a wealth of clues for understanding complex compositions and the formation history of our solar system. The origin of this wide color distribution is still uncertain, but it is likely due to surface ice exposed to ionizing radiation at various levels. Here, we present the spectroscopic evolution of visible reflectance, spectral slopes, and colors from TNO surface ice analogs processed by Galactic cosmic-ray proxy. This study provides compelling evidence that irradiated carbon-containing molecular ices show notable reddening in their visible reflectance spectra. The spectral slopes of processed water ices are neutral and independent of the radiation dose, whereas those of ammonia decrease with the increasing radiation dose. When the carbon-containing molecules are mixed with water and ammonia, the reddening process is found to be neutralized. The irradiation experiments at different temperatures demonstrate that the irradiation temperature could control the reddening efficiency of ices containing carbon and oxygen. For example, the color slopes of pure methanol and carbon dioxide ices significantly increase when the irradiation temperature is 40 K, but there is almost no change at 10 K. This indicates that the color diversity of TNOs can be influenced not only by different levels of radiation exposure but also by varying irradiation temperatures. The data in the current study provide new insights into the influence of initial composition, radiation dose, and irradiation temperature on the color diversity of TNOs, which supply important information for cataloging their surface compositions.

Unified Astronomy Thesaurus concepts: Trans-Neptunian objects (1705); Ice spectroscopy (2250); Surface ices (2117)

1. Introduction

Trans-Neptunian objects (TNOs) represent small icy objects in the outer solar system whose heliocentric orbits hold semimajor axes ranging from Neptune to the Oort cloud, approximately 30–2000 au from the Sun (D. Jewitt & J. Luu 1993; D. K. Prialnik et al. 2020; B. Gladman & K. Volk 2021). An understanding of the physical and chemical properties of these objects is fundamental for comprehending the evolution involved in the early solar nebula, protoplanetary disks around young stars, and the formation of planets (J. X. Luu & D. C. Jewitt 2002; D. Nesvorný et al. 2019). Because TNOs are considered one of the most primitive objects in our solar system without significant heating from the inner solar system, their surface compositions can be used to trace the radiation environment, space-weathering effects, and resurfacing processes in the trans-Neptunian region; these vast realms of space contain abundant clues to untangling the early history of our solar system (M. A. Barucci et al. 2008a; R. Hudson et al. 2008). Due to the large distance from the Sun, TNOs typically have surface temperatures ranging from 30 to 50 K; this results in the condensation of volatile molecules such as water, ammonia, and methanol to form icy surfaces (N. Pinilla-Alonso et al. 2020; L. A. Young et al. 2020). Also, astronomical observations indicate the presence of refractory polymer-like organic residues formed from complex chemical reactions on their surfaces. These organics are thought to be

responsible for the observed ultrared matter (C. Sagan & B. N. Khare 1979; D. P. Cruikshank et al. 2005; R. Brunetto et al. 2006; R. Hudson et al. 2008; C. K. Materese et al. 2014; C. He et al. 2018; E. Quirico et al. 2023; C. Zhang et al. 2023), whose color slope $S' \geq 25\%$ per 100 nm as defined by D. C. Jewitt (2002). However, the precursors of these complex organic molecules have remained elusive. Furthermore, dynamical simulations of our solar system suggest that TNOs are one main source of short-period comets such as 67P/Churyumov-Gerasimenko, some of which are considered delivery systems of biologically important molecules to the early Earth (J. Oró 1961; C. F. Chyba et al. 1990; C. Chyba & C. Sagan 1992; J. R. Cronin & S. Pizzarello 1997; G. Cooper et al. 2001; M. Pasek & D. Lauretta 2008; G. Cooper & A. C. Rios 2016; D. Nesvorný et al. 2017; C. R. Walton et al. 2024). Therefore, studying the chemical evolution of TNOs, particularly the abiotic transformations of simple molecules into prebiotic compounds, such as sugars and nucleobases, is also important to realize the origin of life on Earth (Y.-J. Kuan et al. 2004; K. Altweig et al. 2016; D. P. Cruikshank et al. 2019; Y. Furukawa et al. 2019; Y. Oba et al. 2019; S. A. Sandford et al. 2020). However, the majority of TNOs are very faint, and available observations only permit the identification of simple molecules such as water, methane, carbon monoxide, carbon dioxide, and methanol (M. A. Barucci et al. 2011; E. Fernández-Valenzuela et al. 2021; T. Seccull et al. 2021; M. E. Brown & W. C. Fraser 2023; J. P. Emery et al. 2024; A. C. Souza-Feliciano et al. 2024; M. N. De Prá et al. 2025). Alternatively, considering the lack of correlation between the colors of TNOs and their dynamic properties, along with the fact that varying colors somewhat reflect different compositions in



Original content from this work may be used under the terms of the [Creative Commons Attribution 4.0 licence](#). Any further distribution of this work must maintain attribution to the author(s) and the title of the work, journal citation and DOI.

trans-Neptunian space, these observed colors may serve as a proxy to catalog the complex matter on TNOs (J. Luu & D. Jewitt 1996a; D. C. Jewitt & J. X. Luu 2001; S. Fornasier et al. 2009; M. E. Brown et al. 2011; W. C. Fraser & M. E. Brown 2012; N. Peixinho et al. 2015; F. Merlin et al. 2017; M. E. Schwamb et al. 2019; W. C. Fraser et al. 2021). The color distribution of TNOs is complex and numerous taxonomies have been proposed (C. M. Dalle Ore et al. 2013; R. E. Pike et al. 2017). For example, M. A. Barucci et al. (2005) classified TNOs into four subgroups (BB, BR, IR, and RR) based on the colors derived from BVRIJ photometry. I. Wong & M. E. Brown (2017) defined two classes, red ($R: g-i < 1.2$) and very red ($VR: g-i > 1.2$) using observations in the $ugriz$ magnitude system. A. Thirouin & S. S. Sheppard (2019) divided TNO colors into four groups based on observations through Sloan filters and termed them as neutral, moderately red, very red, and ultrared. The accurate classification of TNOs by surface compositions still needs more data analysis and modeling. Altogether, an understanding of the origin of the color diversity along with the spectroscopic and chemical evolution on TNO surfaces is important to and urgent for the planetary science and astrobiology communities (I. Wong et al. 2019; D. Nesvorný et al. 2020; L. F. Coelho et al. 2022).

The color diversity of TNOs could be associated with particular compounds formed in the protosolar disk or result from complex organic molecules derived from various levels of radiation chemistry (D. C. Jewitt 2002; S. A. Stern 2002; J. F. Cooper et al. 2003; W. M. Grundy 2009; M. E. Brown et al. 2011, 2012; W. C. Fraser & M. E. Brown 2012; C. M. Dalle Ore et al. 2015; E. Quirico et al. 2023). Naturally, intermediate explanations are reasonable with colors influenced both by the initial compositions and by surface modification from energetic particle bombardment (C. M. Dalle Ore et al. 2011; D. Jewitt 2015; I. Wong & M. E. Brown 2016; F. Merlin et al. 2017; E. Quirico et al. 2023; C. Zhang et al. 2023). Several laboratory simulation experiments have been conducted to study how the initial composition and irradiation conditions affect the spectroscopic and color changes of TNO surface-related ices. R. Brunetto et al. (2006) investigated spectral gradients of methane, benzene, and methanol exposed ion radiation at cryogenic temperatures. Their spectra present strong reddening due to the formation of complex organic refractory residues. E. Quirico et al. (2023) found that methanol ice processed by heavy ions can form reddish residues, which might contribute to the reddish surface of Arrokoth. However, N. Sakakibara et al. (2020) demonstrated that the reddish coloration from irradiated methanol and water ice mixtures gradually disappears upon heating to room temperature. This suggests that the ultrared matter on some TNOs might only be stable at low temperatures, unlike well-known nonvolatile refractory organic residues (R. Brunetto et al. 2006; C. K. Materese et al. 2014; C. K. Materese et al. 2015; B. Augé et al. 2016; E. Quirico et al. 2023). M. J. Poston et al. (2018) recorded visible and near-infrared reflectance spectra of ice mixtures composed of water, ammonia, methanol, and hydrogen sulfide to test the hypothesis that the presence or absence of sulfur is essential in the observed bimodal color distribution of Jupiter trojans and TNOs (I. Wong & M. E. Brown 2016). Although the addition of hydrogen sulfide shows noticeable enhancement in the spectral reddening compared to that of ice mixtures without hydrogen sulfide, the complex ice mixtures make it difficult to identify the effect of each component on the

reddening of spectra. Therefore, it is necessary to systematically investigate the visible reflectance, spectral gradients, and colors of TNO ice analogs that have been irradiated, starting from individual components to complex mixtures, which can provide a detailed catalog of the influence of initial composition and radiation dose on the observed color diversity of TNOs.

Here, we conducted comprehensive laboratory simulation experiments to explore the evolution of visible reflectance spectra and colors of TNO ice analogs processed by irradiation under an ultra-high-vacuum condition. Currently observation data from telescopes such as the James Webb Space Telescope (JWST) have identified molecular ices on the surfaces of TNOs including water, methane, ammonia, carbon monoxide, nitrogen, carbon dioxide, methanol, ethane, ethylene, and acetylene along with tentative detection of hydrogen sulfide and silicates (J. R. Brucato et al. 2003; M. E. Brown 2012; D. P. Cruikshank et al. 2015; T. Seccull et al. 2018; M. A. Barucci & F. Merlin 2020; W. M. Grundy et al. 2020; A. Mahjoub et al. 2021; M. E. Brown & W. C. Fraser 2023; J. P. Emery et al. 2024; T. Seccull et al. 2024; M. N. De Prá et al. 2025). We select ices 1–36 composed of water, methane, ammonia, carbon monoxide, carbon dioxide, and methanol (Table 1) as the initial surface composition of airless TNOs and process them by energetic electrons to mimic the ionizing-radiation exposure on the surface of TNOs (W. Zheng et al. 2008; R. I. Kaiser et al. 2011; Y. S. Kim & R. I. Kaiser 2012; B. M. Jones & R. I. Kaiser 2013; M. Forstel et al. 2016; A. M. Turner & R. I. Kaiser 2020; A. M. Turner et al. 2021; N. F. Kleimeier et al. 2022). The highly energetic electrons simulate the secondary electrons formed in the track of Galactic cosmic rays (GCRs) penetrating the ice; the interaction between these electrons and molecules essentially controls the chemical reactions within icy mantles (R. E. Johnson 1990; C. J. Bennett et al. 2005). Considering that the laboratory radiation dose is similar to the dose accumulated on TNOs over approximately 1800 million years (J. F. Cooper et al. 2003; G. Strazzulla et al. 2003; R. Hudson et al. 2008), this provides the potential to reconstruct photometric observations of objects in the outer solar system and allows us to probe how the chemical evolution affects the color diversity of TNOs. The processing temperature of ices is kept at 40 K, which coincides with the temperature range of 30–50 K for TNOs (L. A. Young et al. 2020). The volatile molecules of methane and carbon monoxide cannot condense at this temperature (C. J. Bennett et al. 2004; C. J. Bennett et al. 2006); therefore, ice mixtures containing methane and carbon monoxide are processed at 20 K. In addition, the irradiation temperature can control the class of products and influence the spectral slopes. We also record the reflectance spectra of ices irradiated at 10 K to study the influence of irradiation temperature on the reddening of spectral slopes. Further, ices processed at 10 K are also highly relevant to the surface compositions of TNOs with a lower average temperature than 20 K, such as Sedna (S. M. Menten et al. 2022). Systematically studying the visible reflectance spectral evolution of TNO ice analogs will provide important information to inventory the complex compositions underlying the color diversity of TNOs.

2. Experimental Methods

The irradiation experiments were conducted in an ultra-high-vacuum chamber at pressures of a few 10^{-11} Torr achieved by magnetically suspended turbomolecular pumps backed by oil-free

Table 1
Experimental Parameters of the Ices, Ratio, and Temperatures Used in This Work

Ice No.	Composition	Ratio	Temperature (K)	Color Slope before Irradiation (% per 100 nm)	Color Slope after Irradiation (% per 100 nm)	Color Slope at 320 K (% per 100 nm)
1	H ₂ O	...	40	4.9 ± 1.6	6.1 ± 1.8	0.7 ± 1.9
2	H ₂ O	...	10	3.4 ± 0.9	3.3 ± 1.1	0.05 ± 0.5
3	NH ₃	...	40	12.4 ± 1.1	1.0 ± 0.6	5.9 ± 1.7
4	NH ₃	...	10	14.0 ± 1.6	7.2 ± 1.4	2.4 ± 1.4
5	¹³ CO ₂	...	40	9.4 ± 1.6	24.4 ± 2.2	-1.0 ± 0.4
6	¹³ CO ₂	...	10	9.1 ± 1.8	7.9 ± 1.3	-0.9 ± 0.3
7	H ₂ O: ¹³ CH ₄	(1.8 ± 0.2):1	20	10.9 ± 0.8	4.4 ± 1.6	4.8 ± 1.5
8	H ₂ O: ¹³ CH ₄	(1.7 ± 0.2):1	10	13.1 ± 0.9	4.8 ± 1.3	4.8 ± 1.2
9	H ₂ O:NH ₃	(2.8 ± 0.2):1	40	2.8 ± 0.5	10.3 ± 1.5	1.9 ± 0.5
10	H ₂ O:NH ₃	(2.6 ± 0.2):1	10	6.3 ± 0.5	8.8 ± 1.0	1.3 ± 0.4
11	H ₂ O: ¹³ CO	(1.1 ± 0.2):1	20	4.2 ± 0.9	10.4 ± 1.3	3.9 ± 1.3
12	H ₂ O: ¹³ CO	(1.7 ± 0.2):1	10	14.8 ± 0.5	12.1 ± 0.8	1.5 ± 0.6
13	H ₂ O: ¹³ CO ₂	(1.2 ± 0.2):1	40	12.5 ± 0.8	12.1 ± 0.8	-1.3 ± 0.4
14	H ₂ O: ¹³ CO ₂	(1.2 ± 0.2):1	10	8.9 ± 0.9	10.8 ± 0.8	-0.9 ± 0.4
15	H ₂ O: ¹³ CH ₃ OH	(1.0 ± 0.2):1	40	10.3 ± 0.8	6.9 ± 1.7	13.9 ± 2.0
16	H ₂ O: ¹³ CH ₃ OH	(0.8 ± 0.2):1	10	2.0 ± 0.6	7.7 ± 0.9	10.2 ± 2.5
17	¹³ CH ₄ : NH ₃	(1.8 ± 0.2):1	20	6.1 ± 0.6	18.1 ± 3.2	13.6 ± 6.3
18	¹³ CH ₄ :NH ₃	(1.7 ± 0.2):1	10	0.4 ± 0.8	24.7 ± 4.6	16.8 ± 4.0
19	¹³ CH ₄ : ¹³ CO	(1.0 ± 0.2):1	20	4.1 ± 0.6	23.2 ± 4.5	21.4 ± 4.8
20	¹³ CH ₄ : ¹³ CO	(1.1 ± 0.2):1	10	3.9 ± 0.7	19.4 ± 4.6	17.2 ± 4.3
21	¹³ CH ₄ : ¹³ CO ₂	(1.1 ± 0.2):1	20	7.6 ± 0.5	12.7 ± 1.9	12.7 ± 2.5
22	¹³ CH ₄ : ¹³ CO ₂	(1.2 ± 0.2):1	10	4.9 ± 0.5	32.1 ± 1.9	24.4 ± 1.8
23	¹³ CH ₄ : ¹³ CH ₃ OH	(2.2 ± 0.2):1	20	2.6 ± 0.5	18.9 ± 5.8	11.5 ± 6.9
24	¹³ CH ₄ : ¹³ CH ₃ OH	(0.8 ± 0.2):1	10	4.6 ± 0.5	20.3 ± 4.1	9.7 ± 4.3
25	NH ₃ : ¹³ CO	(0.4 ± 0.2):1	20	3.6 ± 0.7	10.0 ± 1.8	4.5 ± 0.9
26	NH ₃ : ¹³ CO	(0.4 ± 0.2):1	10	3.2 ± 1.1	30.0 ± 1.7	3.7 ± 2.1
27	NH ₃ : ¹³ CO ₂	(0.6 ± 0.2):1	40	14.1 ± 0.8	11.5 ± 0.8	-0.3 ± 0.3
28	NH ₃ : ¹³ CO ₂	(0.6 ± 0.2):1	10	11.7 ± 0.9	15.9 ± 1.0	-0.8 ± 0.5
29	NH ₃ : ¹³ CH ₃ OH	(0.3 ± 0.2):1	40	6.5 ± 0.9	20.3 ± 3.5	9.8 ± 4.7
30	NH ₃ : ¹³ CH ₃ OH	(0.3 ± 0.2):1	10	9.2 ± 1.8	10.1 ± 3.1	18.1 ± 4.8
31	¹³ CO: ¹³ CO ₂	(1.0 ± 0.2):1	20	12.4 ± 0.8	9.9 ± 0.6	-1.3 ± 0.5
32	¹³ CO: ¹³ CO ₂	(1.0 ± 0.2):1	10	13.0 ± 0.8	10.3 ± 0.7	-1.5 ± 0.4
33	¹³ CO: ¹³ CH ₃ OH	(1.1 ± 0.2):1	20	3.2 ± 0.3	14.2 ± 2.9	...
34	¹³ CO: ¹³ CH ₃ OH	(1.0 ± 0.2):1	10	2.6 ± 0.4	14.2 ± 1.4	0.1 ± 1.1
35	¹³ CO ₂ : ¹³ CH ₃ OH	(1.2 ± 0.2):1	40	4.7 ± 0.6	14.1 ± 1.9	2.2 ± 0.7
36	¹³ CO ₂ : ¹³ CH ₃ OH	(1.2 ± 0.2):1	10	3.7 ± 0.5	35.9 ± 1.1	8.7 ± 1.6

Note. All ices have a thickness of 850 ± 50 nm with dose accumulation up to 82 ± 10 eV amu⁻¹ and are then warmed up to 320 K at 1 K min⁻¹.

scroll pumps, and have been described elsewhere (B. M. Jones & R. I. Kaiser 2013; A. M. Turner & R. I. Kaiser 2020; C. Zhang et al. 2023). Briefly, a polished silver wafer coated with rhodium is attached to an oxygen-free high conductivity copper cryostat via indium foil and connected to a two-stage closed-cycle helium refrigerator (CTI-Cryogenics Cryodyne 1020; CTI-Cryogenics 9600 compressor). The temperature of the silver wafer is monitored by a silicon diode sensor (Lakeshore DT-470) and regulated in a range of 5–320 K with a precision of ± 0.3 K by a programmable temperature controller (Lakeshore 336). The TNO ice analogs were prepared through introducing high-purity methane (¹³CH₄, 99% atom ¹³C, Sigma Aldrich), water (H₂O, HPLC, Fisher Chemical), ammonia (NH₃, 99.9992%, Matheson), carbon monoxide (¹³CO, 99% atom ¹³C, Sigma Aldrich), carbon dioxide (¹³CO₂, 99% atom ¹³C, Sigma Aldrich), and methanol (¹³CH₃OH, Sigma Aldrich, 99.9%) at pressures of 3×10^{-8} Torr in the chamber and followed by deposition on the wafer via the glass capillary array. Here, we use carbon-13-labeled reactants to eliminate potential contaminants. The thickness (d) of each ice system is estimated with Equation (1) (O. S. Heavens 1955; A. M. Turner et al. 2015), where N is the number of interference fringes recorded during ice deposition, n is the ice's refractive

index at 632.8 nm, and $\theta \approx 4^\circ$ is the angle of light incidence:

$$d = \frac{N\lambda}{2\sqrt{n^2 - \sin^2 \theta}}. \quad (1)$$

The thicknesses of ices were controlled to be 850 ± 50 nm by monitoring the number of fringes during deposition (A. M. Turner et al. 2015). The refractive indices for pure ices used here are listed in Table 2, and those of binary ice mixtures are obtained by averaging the refractive index of two components. To systematically understand the evolution of visible reflectance (color) induced by ionizing radiation at low temperatures, molecules identified on TNOs (methane, water, ammonia, carbon monoxide, carbon dioxide, and methanol) along with their bicomponent ice mixtures were selected for this work (M. A. Barucci et al. 2011; M. E. Brown 2012; M. A. Barucci & F. Merlin 2020; M. E. Brown & W. C. Fraser 2023; M. N. De Prá et al. 2025). It is worth noting that silicates are also possibly present in the trans-Neptunian region and exhibit “red” spectral slopes (J. R. Brucato et al. 2003; T. Seccull et al. 2018). However, it is not the aim of this study to prepare all possible compounds

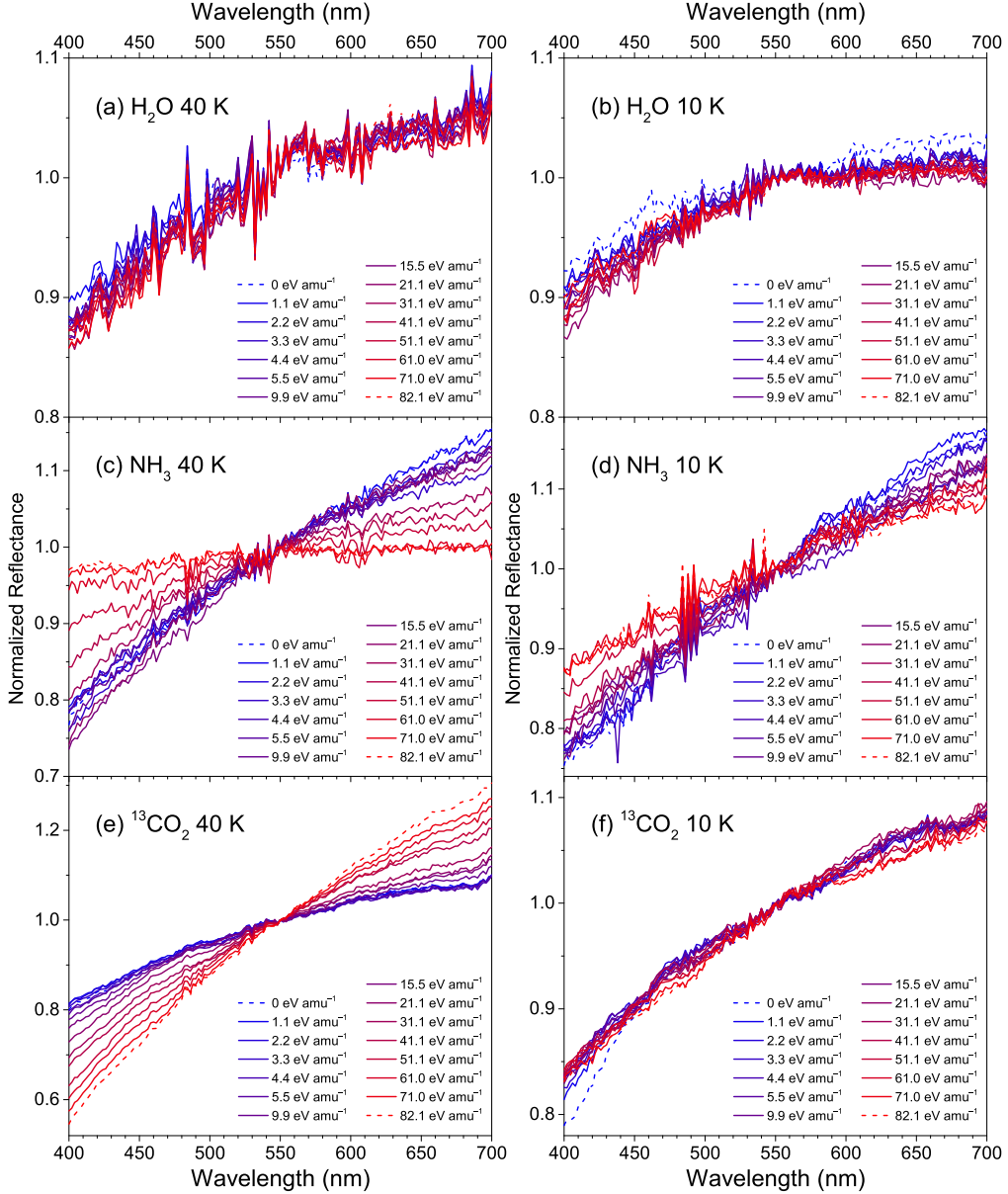


Figure 1. The visible reflectance spectra of ices 1–6 measured during the irradiation. Ices 1–6 in Table 1 are displayed in the order of (a)–(f). All spectra are normalized at 550 nm and plotted as a gradient color from blue to red as radiation dose increases. Dashed lines represent the spectra of ices before and after irradiation.

simultaneously and the study should start from simple ices before moving to complex mixtures.

After deposition, ices were isothermally processed by 5 keV electrons (Specs EQ 22–35 electron source) to simulate the secondary electrons formed in the track of GCRs penetrating the ices. The electron incidence angle is 70° to the ice-surface normal. Utilizing Monte Carlo simulations (CASINO 2.42; D. Drouin et al. 2007), the maximum depths of the electron penetration were estimated to be about 600 ± 50 nm, which is less than the ice thickness of 850 ± 50 nm, thus avoiding interaction between high-energy electrons and the coated rhodium surface. The dose accumulation within processed ices was controlled to be about 82 ± 10 eV amu⁻¹ (C. Zhang et al. 2023; C. Zhang et al. 2024). Note that to enable the comparison between our results and the dose accumulation within trans-Neptunian space, we provide the unit of the deposited dose in eV amu⁻¹, which is widely adopted in the astronomy community (C. J. Bennett et al. 2013; A. Yeghikyan 2017;

Table 2
Refractive Indices (n) Are Used to Determine the Thickness of Ices in This Study (M. Bouilloud et al. 2015).

Ice	n
H ₂ O	1.27 ± 0.02
¹³ CH ₄	1.34 ± 0.04
NH ₃	1.33 ± 0.04
¹³ CO	1.25 ± 0.03
¹³ CO ₂	1.27 ± 0.02
¹³ CH ₃ OH	1.33 ± 0.04

E. Quirico et al. 2023). This unit can be converted to eV molecule⁻¹ used in the astrochemistry community by multiplying the units of eV amu⁻¹ by the molecular mass of the reactants, e.g., 18 amu molecule⁻¹ for water. Objects in trans-Neptunian space undergo continuous exposure to ionizing radiation including ultraviolet (UV) photons, charged

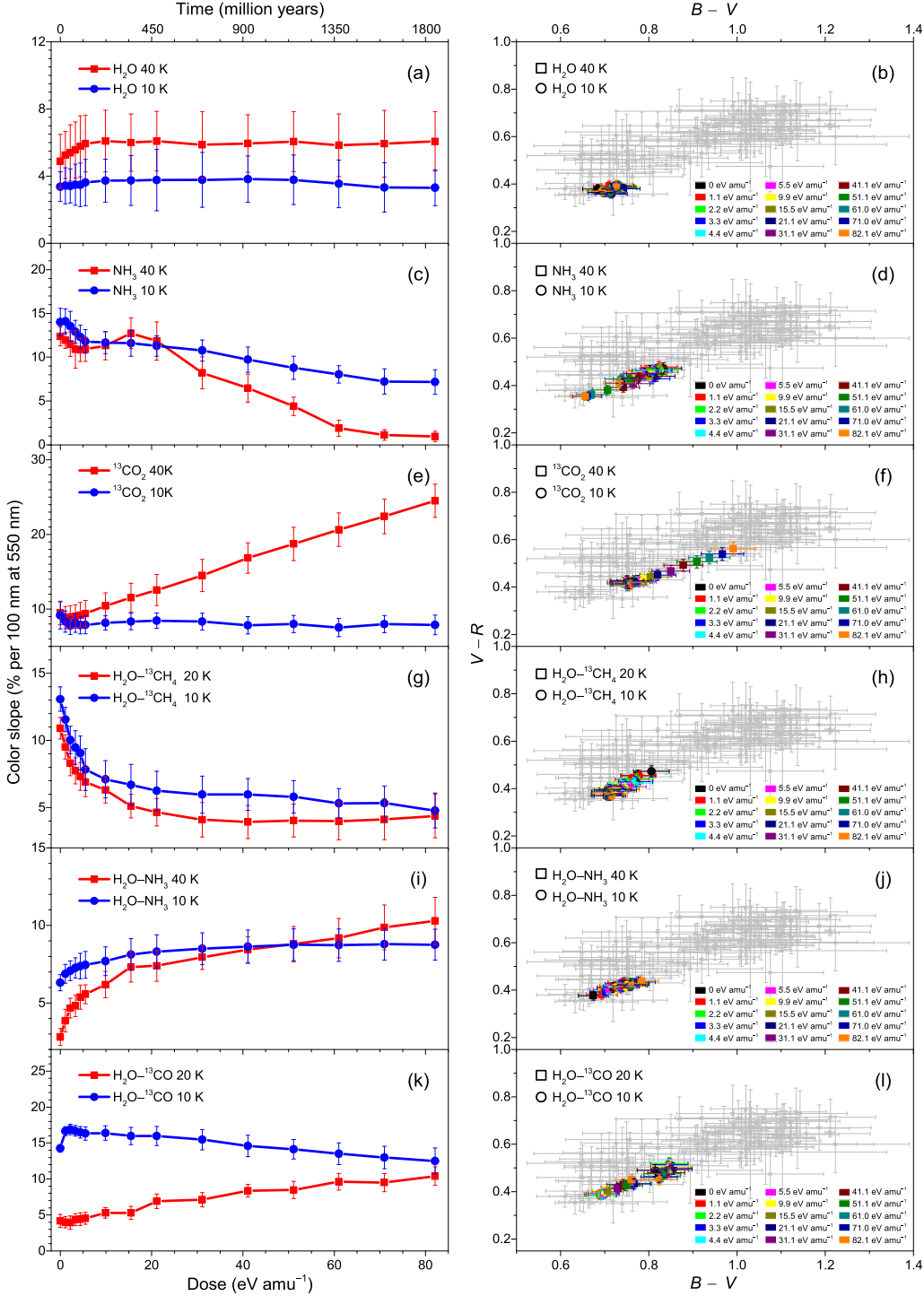


Figure 2. The color slope and color evolution of ices 1–12 as the radiation dose increases, sequenced in panels (a)–(l). Error bars shown are from linear fitting of spectra. The gray area is the colors of TNOs from observations (O. R. Hainaut et al. 2012).

particles originating from solar winds, and GCRs (R. E. Johnson 1991; J. F. Cooper et al. 2003). Among those sources of ionizing radiation, charged particles consist of more than 90% protons (H^+) and 1%–10% helium nuclei (He^{2+}), with solar wind particles typically having energies in the range of a few keV and GCR particles reaching energies in the hundreds of MeV (R. E. Johnson 1990; G. J. Golabek & M. Jutzi 2021). The UV radiation exhibits a flux of about 10^3 photons $cm^{-2} s^{-1}$ with energies lower than 20.0 eV (S. S. Prasad & S. P. Tarafdar 1983). The chemistry of airless TNO surfaces is predominantly

controlled by secondary electrons, generated by ionizing-radiation-penetrating ices. Essentially, implanted protons transfer their kinetic energy to the electronic system of target molecules, leading to the generation of electrons with energies up to a few keV (G. Strazzulla et al. 2003; C. J. Bennett et al. 2005). The electronic linear energy transfer of MeV protons to molecules within such ices exhibits a similar value of a few keV μm^{-1} as the 5 keV electrons used in the present experiments (B. M. Jones & R. I. Kaiser 2013). In addition, previous research has shown that radiation products from interstellar ices are weakly

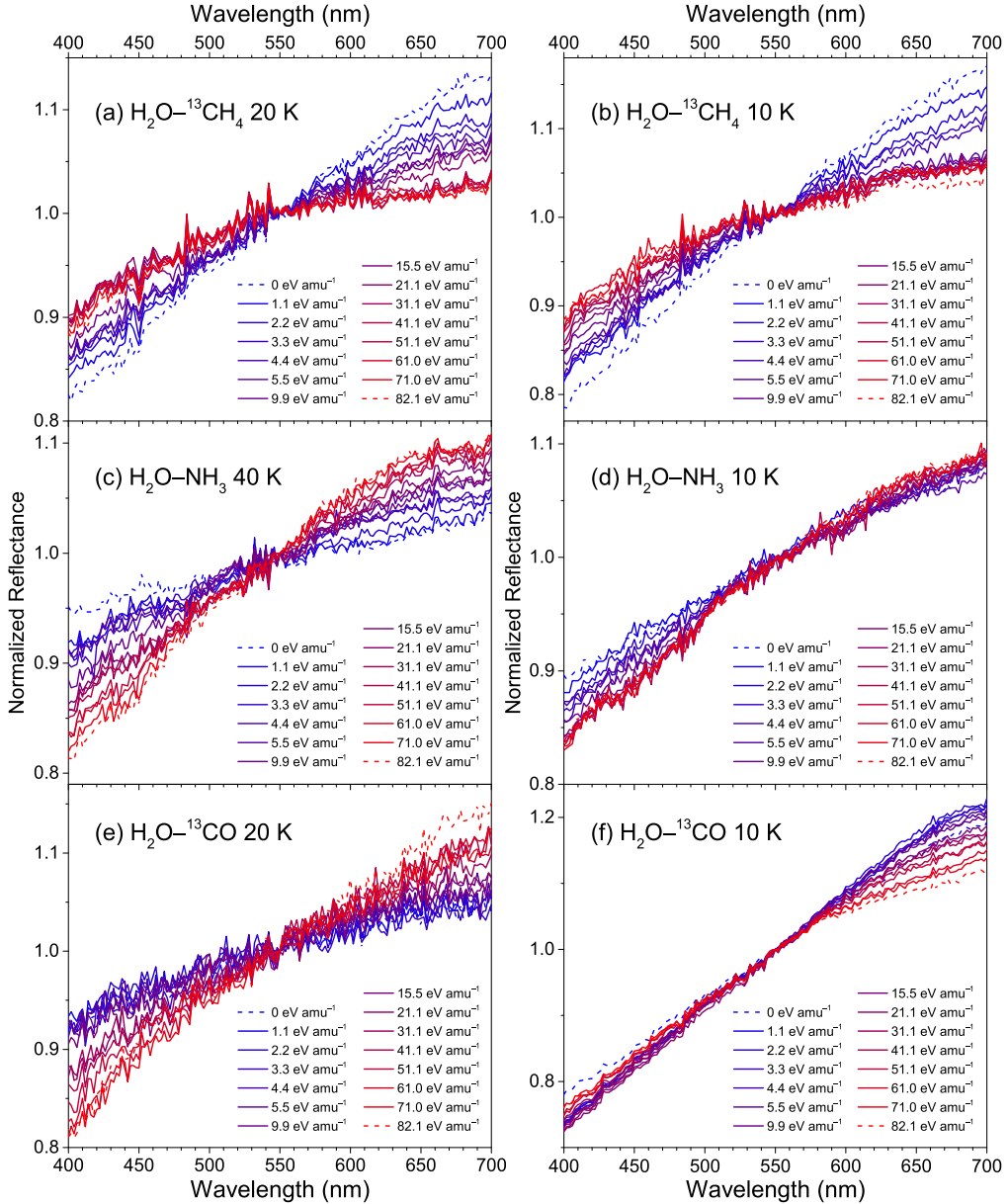


Figure 3. The visible reflectance spectra of ices 7–12 measured during the irradiation. Ices 7–12 in Table 1 are displayed in the order of (a)–(f). All spectra are normalized at 550 nm and plotted as a gradient color from blue to red as radiation dose increases. Dashed lines represent the spectra of ices before and after irradiation.

dependent on the type of irradiation whether electrons, heavy ions, or UV photons (G. A. Baratta et al. 2002; G. M. Muñoz Caro et al. 2014; K. I. Oberg 2016; M. J. Abplanalp et al. 2018; C. R. Arumainayagam et al. 2019). Our laboratory experiments mimic the formation of complex products in molecular ices at low temperatures through charged particles via electronic energy-loss processes on airless TNOs. After irradiation, temperature-programmed desorption (TPD) studies were carried out by heating the substrate to 320 K at a rate of 1 K minute⁻¹.

The reflectance spectra of ices were collected *in situ* by an ultraviolet-visible (UV-vis) spectrometer (Thermo Scientific Evolution 300) during irradiation and TPD duration. The focused light from the UV-vis spectrometer was reflected from the ices at an angle of 30° and focused onto a photodiode shielded from ambient light. The UV-vis reflectance spectra in the 190–1100 nm range were recorded with a 2 nm data-point spacing. The spectrum before ice deposition was recorded as background and subtracted when UV-vis reflectance spectra

were measured. In some cases, the UV-vis reflectance spectra are superimposed by strong interference features due to slight alteration of the thickness and refractive index during the irradiation, and a simple subtraction of the two spectra cannot be applied to remove the interference bands. To obtain experimental UV-vis spectra free from interference patterns, the interference pattern was derived theoretically by employing a “two interfaces between three media” model generalized for complex refractive indices $n_i + ik_i$ (G. Tarczay et al. 2016). To compare UV-vis reflectance spectra measured here with astronomical observations, the visible range (400–700 nm) was normalized concerning the reflectance at 550 nm, which is widely used for the data from photometry results of TNOs (J. Luu & D. Jewitt 1996a; D. C. Jewitt & J. X. Luu 2001; M. A. Barucci et al. 2005; S. Fornasier et al. 2009; F. Merlin et al. 2017). The color slopes S' (% per 100 nm) were calculated through Equation (2) defined in the literature (J. X. Luu & D. C. Jewitt 1990; D. C. Jewitt 2002) with

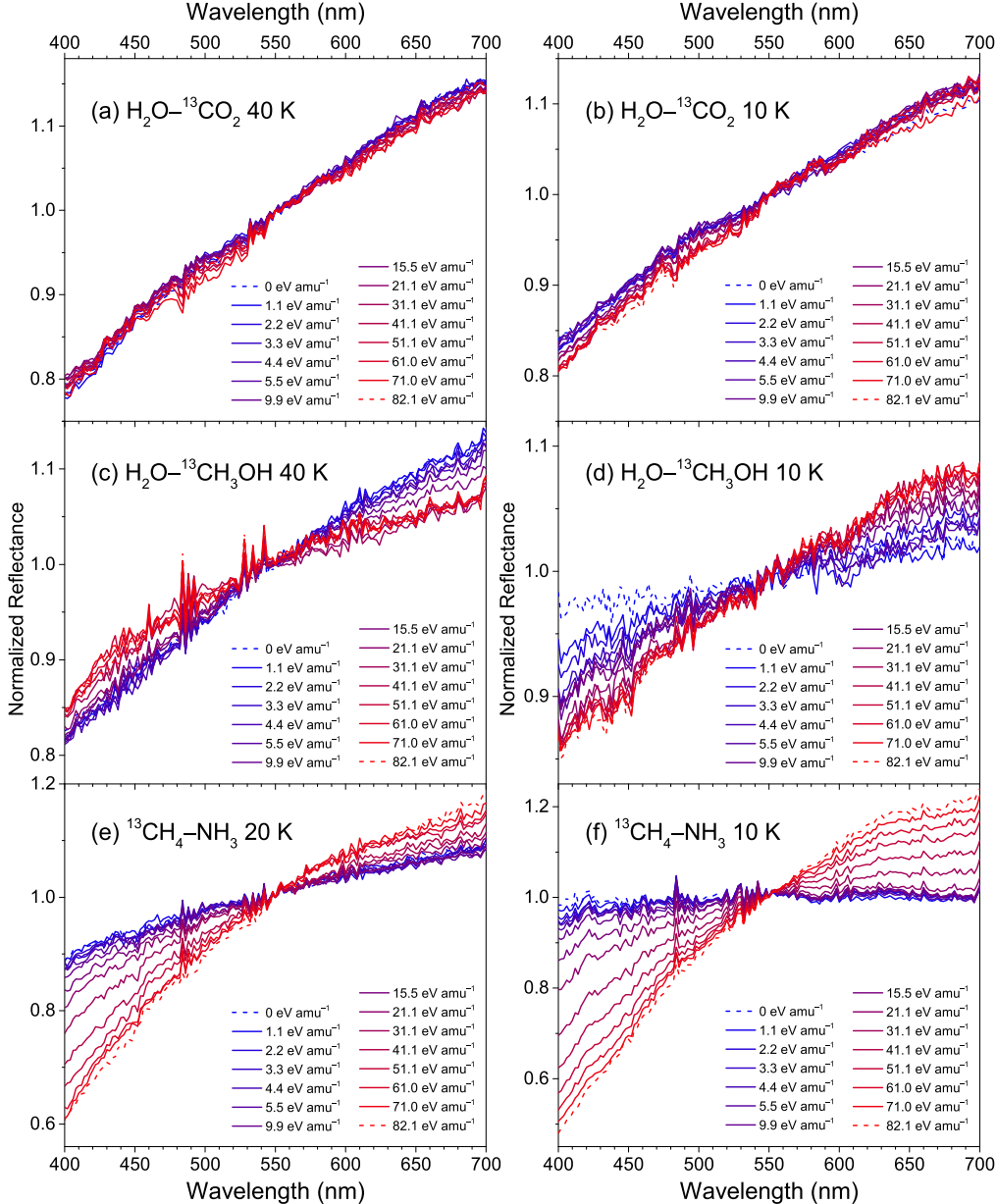


Figure 4. The visible reflectance spectra of ices 13–18 measured during the irradiation. Ices 13–18 in Table 1 are displayed in the order of (a)–(f). All spectra are normalized at 550 nm and plotted as a gradient color from blue to red as radiation dose increases. Dashed lines represent the spectra of ices before and after irradiation.

reflectance R of the visible spectrum at the wavelength λ (nm):

$$S' = \frac{dR/d\lambda}{R_{550 \text{ nm}}}. \quad (2)$$

Table 1 lists all the color slopes of ices 1–36 before and after irradiation and after heating to 320 K. Besides the color slopes, we also estimated the color, which is defined as the difference in magnitude of radiant flux (logarithmic scale) between two different filters in astronomy. For the spectrum of an astronomical object in the solar system, the color index is determined via Equation (3) (J. X. Luu & D. C. Jewitt 1990; D. C. Jewitt 2002),

$$B - V = (B - V)_{\text{Sun}} + 2.5 \log \left(\frac{2 + S' \Delta \lambda}{2 - S' \Delta \lambda} \right) \quad (3)$$

where $B - V$ is the color of the astronomical object through B and V filters, $(B - V)_{\text{Sun}}$ is the reference color of the Sun (J. Holmberg et al. 2006), and $\Delta \lambda$ is the difference between the central wavelengths of the B and V filters, with filter ranges of 400–500 nm (B) and 500–600 nm (V). The $V - R$ color through V and R filters with wavelength ranges 500–600 nm (V) and 600–700 nm (R) were also estimated.

3. Results and Discussion

3.1. Neat Ices

3.1.1. Water

Water is one of the most widespread molecular ices on TNOs (M. A. Barucci et al. 2008b; M. A. Barucci et al. 2011; M. A. Barucci & F. Merlin 2020), and previous irradiation

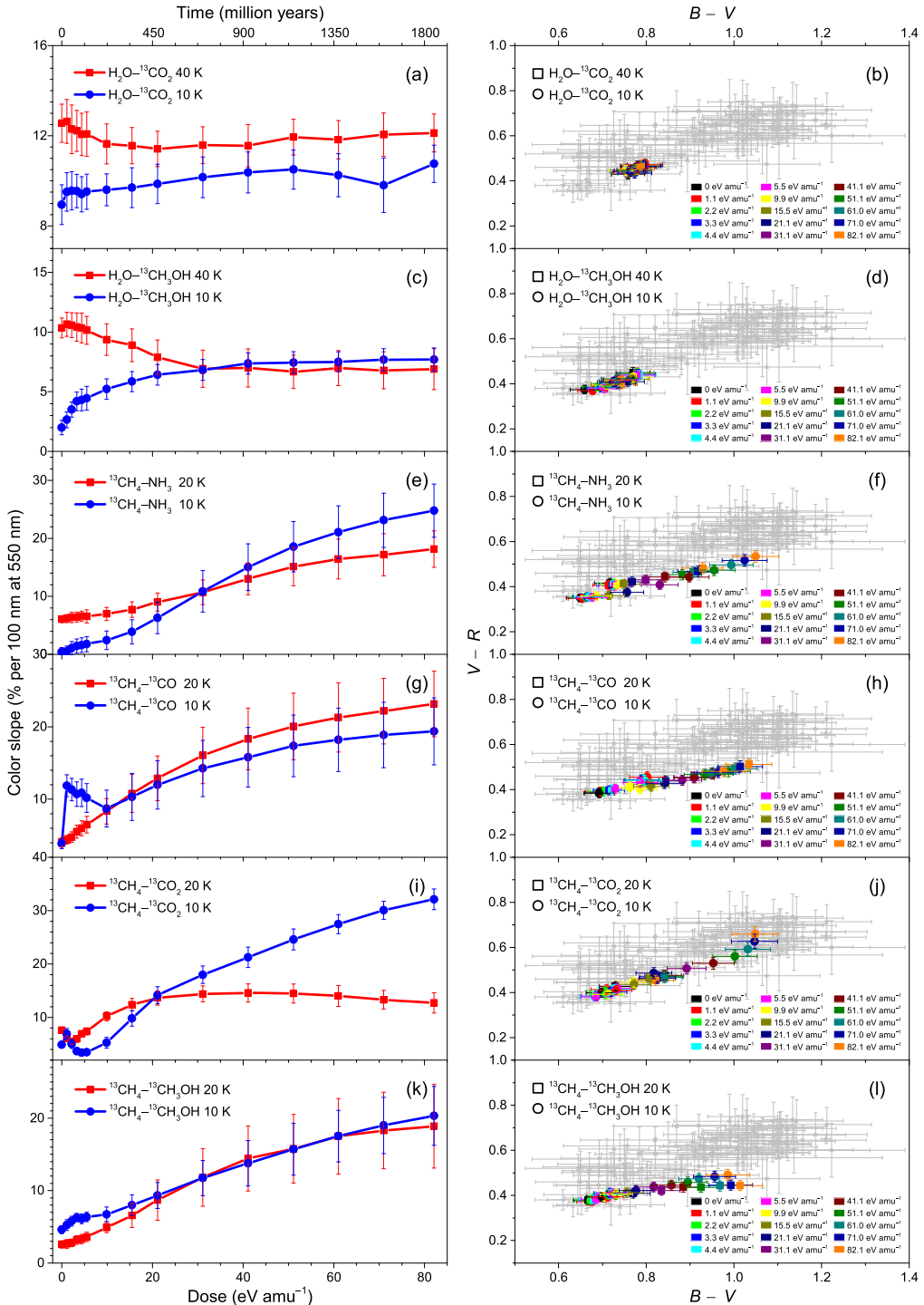


Figure 5. The color slopes and color evolution of ices 13–24 as the radiation dose increases, sequenced in panels (a)–(l). Error bars shown are from linear fitting of spectra. The gray area is the colors of TNOs from observations (O. R. Hainaut et al. 2012).

experiments showed that the major products from processed water ice are hydrogen (H_2), oxygen (O_2), and hydrogen peroxide (H_2O_2) formed predominantly through radical–radical reactions (W. Zheng et al. 2006a, 2006b). The visible reflectance spectra of water at both temperatures exhibit a radiation-dose-independent behavior (Ices 1 and 2, Figures 1(a) and (b)). As the radiation dose increases, the color slopes keep at about 6% per 100 nm at 40 K and about 3% per 100 nm at 10 K (Figure 2(a)). The colors of processed water ice are about 0.72 of $B - V$ and 0.38 of $V - R$ (Figure 2(b)), which suggests

that the water-dominated TNOs might be observed as neutral colors, such as the bowl-type TNOs observed by JWST (M. N. De Prá et al. 2025; N. Pinilla-Alonso et al. 2025).

3.1.2. Ammonia

Ammonia has a sublimation line near 34 au. Therefore, this molecule can be retained on small TNOs by mixing with other compounds and potentially influence their surface colors (M. E. Brown et al. 2011). An absorption feature observed at 2.2 μm in the spectra of Charon and Orcus is probably from

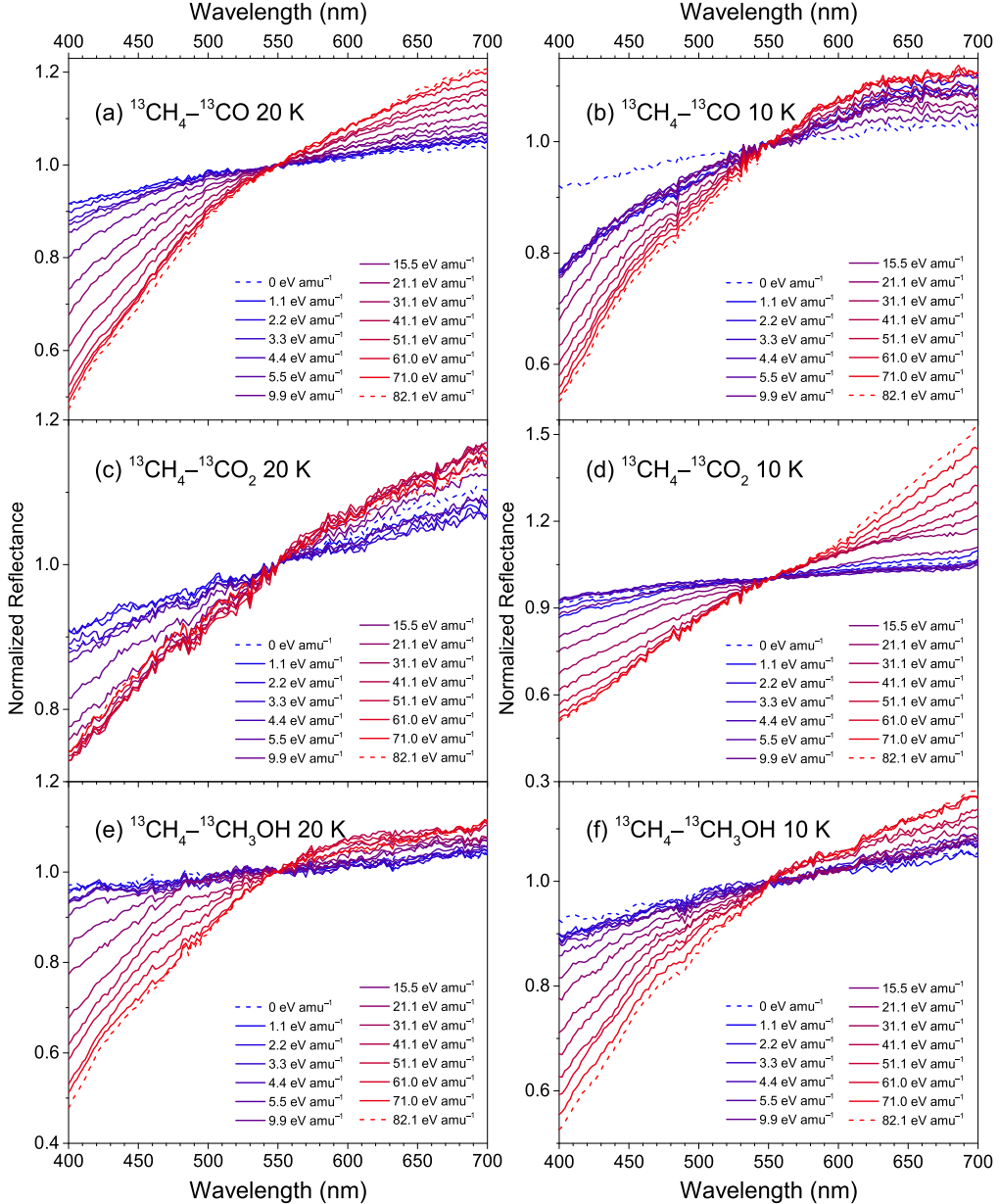


Figure 6. The visible reflectance spectra of ices 19–24 measured during the irradiation. Ices 19–24 in Table 1 are displayed in the order of (a)–(f). All spectra are normalized at 550 nm and plotted as a gradient color from blue to red as radiation dose increases. Dashed lines represent the spectra of ices before and after irradiation.

ammonia and its derivatives (M. A. Barucci et al. 2008c; F. Merlin et al. 2010; F. E. DeMeo et al. 2015; J. C. Cook et al. 2023). Surprisingly, the visible reflectance spectra of ammonia at 40 K become flat as the radiation dose increases (Ice 3, Figure 1(c)). The color slopes before 15 eV amu^{-1} are about 12% per 100 nm and then decrease to 1% per 100 nm as the radiation dose accumulates to 82 eV amu^{-1} (Figure 2(c)). At 10 K, the spectra gradually change to less steep (Ice 4, Figure 1(d)) and the color slopes fall from 14% per 100 nm to 7% per 100 nm during the irradiation (Figure 2(c)). Ammonia ices irradiated at these two temperatures have similar values of color slopes during the low-dose range ($< 21 \text{ eV amu}^{-1}$). But in the high-dose region, color slopes at 40 K decrease faster than those at 10 K. Their colors shift toward the neutral direction during irradiation (Figure 2(d)). This study suggests that ammonia ices on TNOs can lead to neutral colors when exposed to ionizing-radiation environment.

3.1.3. Carbon Dioxide

Carbon dioxide in solid form has been recently confirmed on TNOs by JWST (M. E. Brown & W. C. Fraser 2023; A. C. Souza-Feliciano et al. 2024; M. N. De Prá et al. 2025) as well as on centaurs (O. H. Pinto et al. 2023). The visible reflectance spectra of carbon dioxide ice at 40 K change to be steeper during the irradiation (Ice 5, Figure 1(e)). The color slopes monotonically rise to about 24% per 100 nm from 9% per 100 nm (Figure 2(e)). However, the spectra of carbon dioxide irradiated at 10 K are independent of the radiation dose (Ice 6, Figure 1(f)) with color slopes about 8% per 100 nm (Figure 2(e)). The colors of carbon dioxide ice at 40 K are in the range of 0.77–1.00 for $B - V$ and 0.43–0.56 for $V - R$ (Figure 2(f)). At 10 K, the colors have $V - R$ values about 0.75 and $V - R$ about 0.42. These findings suggest that carbon dioxide ice exposed to ionizing radiation in a “warmer”

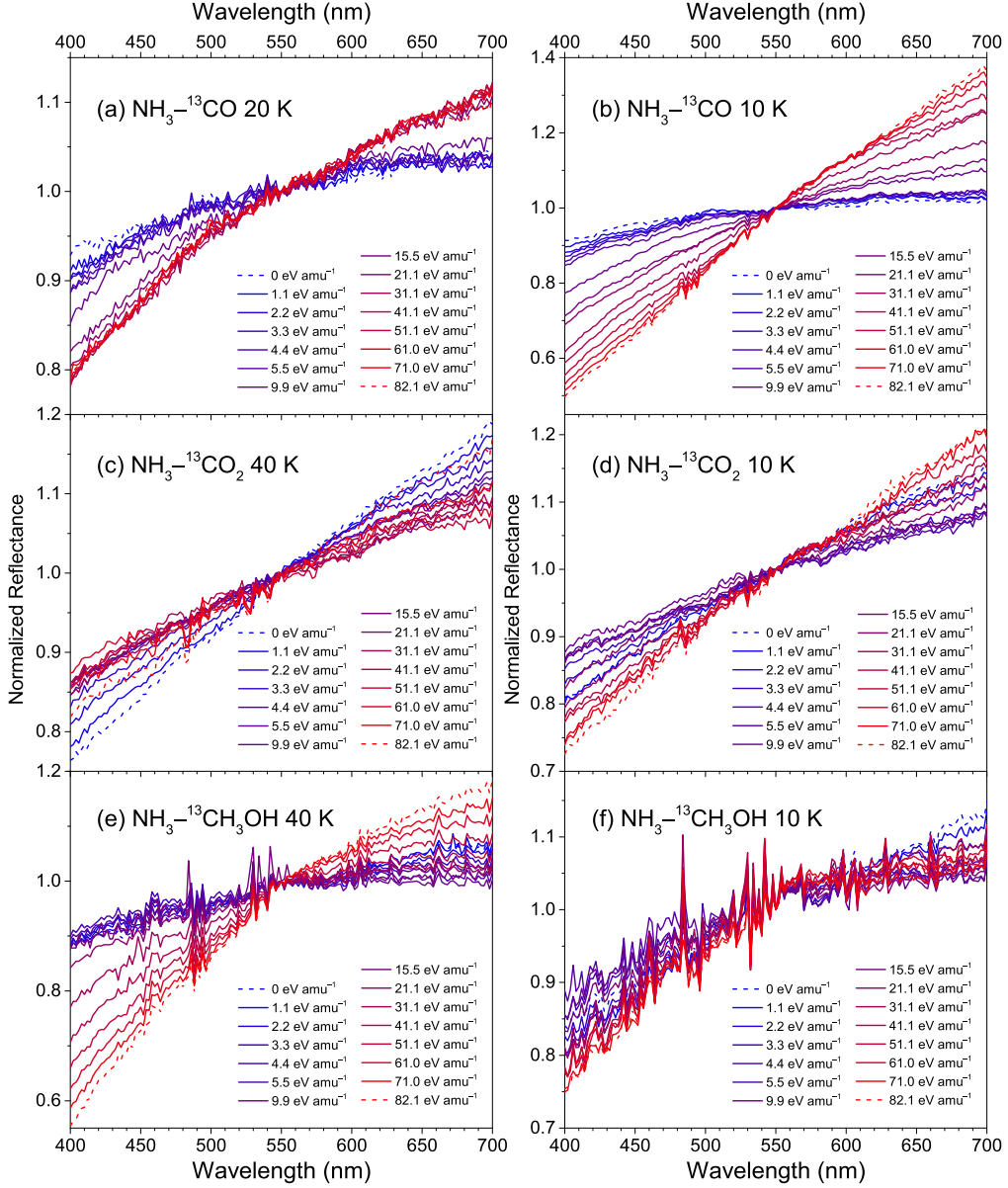


Figure 7. The visible reflectance spectra of ices 25–30 measured during the irradiation. Ices 25–30 in Table 1 are displayed in the order of (a)–(f). All spectra are normalized at 550 nm and plotted as a gradient color from blue to red as radiation dose increases. Dashed lines represent the spectra of ices before and after irradiation.

environment can contribute to the reddening of visible spectra of TNOs, such as 2004 PG115 (O. R. Hainaut et al. 2012).

For other individual ices, previous reports have found that processed methane ices at 10 K and 20 K have similar tendencies with color slopes from almost zero to 18% per 100 nm (C. Zhang et al. 2023). The color slopes of irradiated carbon monoxide ices at 20 K increase to 12% per 100 nm and 35% per 100 nm at 10 K. For methanol ices irradiated at 40 K, the color slopes initially decrease from 19% to 15% per 100 nm and then increase to 32% per 100 nm. At 10 K, the color slopes stay around 13% per 100 nm as the radiation dose increases (C. Zhang et al. 2024).

3.2. Binary Ice Mixtures

During the irradiation experiments, the visible reflectance spectra of ices of methane, ammonia, carbon monoxide, carbon dioxide, and methanol mixed with water (Ices 7–16) only show slight changes with various patterns (Figures 3(a)–(f) and 4(a)–(d)).

The color slopes of water–methane ice mixtures drop to about 5% per 100 nm from about 12% per 100 nm (Figure 2(g)), in which color slopes before 21 eV amu⁻¹ fall faster than that in the high-dose region. For water–ammonia ice mixtures, as radiation dose increases, color slopes at 40 K increase to 10% per 100 nm from 3% per 100 nm and at 10 K stay around 8% per 100 nm (Figure 2(i)). The color slopes of irradiated water and carbon monoxide ice mixtures at 20 K go to 10% per 100 nm from 4% per 100 nm (Figure 2(k)). At 10 K, the color slopes initially have a value of 15% per 100 nm and then reduce to 12% per 100 nm (Figure 2(k)). Ice mixtures composed of water and carbon dioxide present independent color slopes to radiation dose, which are about 12% per 100 nm at 40 K and 10% per 100 nm at 10 K (Figure 5(a)). The color slopes of water–methanol ice mixtures at 40 K decrease to 7% per 100 nm from 10% per 100 nm as the radiation dose goes up to 31 eV amu⁻¹, and then level off (Figure 5(c)). At 10 K, the color slopes increase to about 8% per 100 nm before 31 eV amu⁻¹, and then remain constant

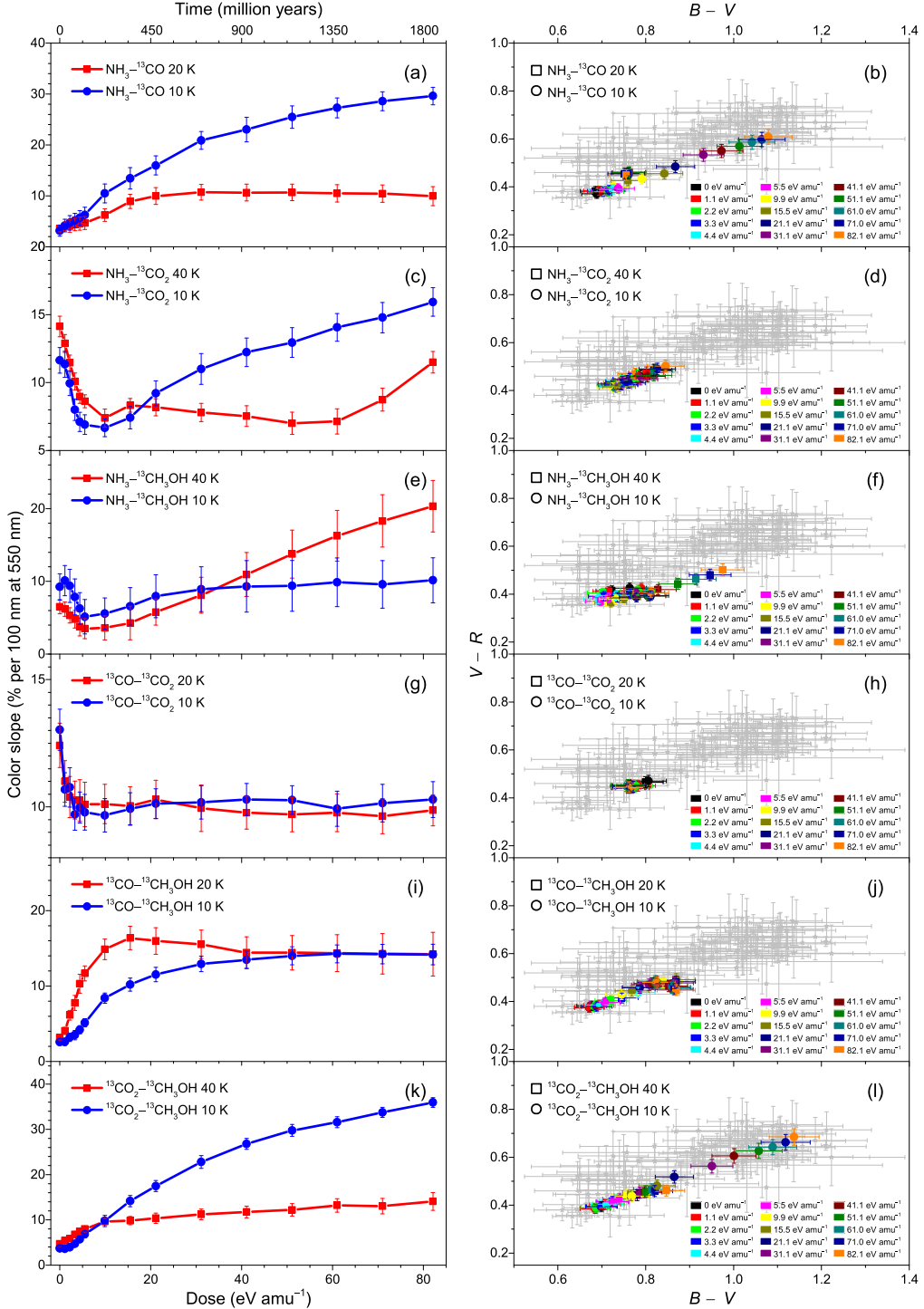


Figure 8. The color slope and color evolution of ices 25–36 as the radiation dose increases, sequenced in panels (a)–(l). Error bars shown are from linear fitting of spectra. The gray area is the colors of TNOs from observations (O. R. Hainaut et al. 2012).

(Figure 5(c)). The colors of these ice mixtures are all in the neutral position within the range of 0.65–0.86 for $B - V$ and 0.37–0.51 for $V - R$ (Figures 2(h), (j), and (l), Figures 5(b) and (d)). These findings suggest that the water can prevent the reddening effect from irradiation on pure methane, carbon monoxide, carbon dioxide, and methanol ices, and counteract the reactions that make the color slopes of ammonia ice decrease. The influence of water molecules on the color of these irradiated ice mixtures suggests that the water-dominated TNOs are more likely to show a neutral color. This agrees with the observation data that indicates most

neutral TNOs have a water-rich surface (M. A. Barucci et al. 2005; M. A. Barucci et al. 2011; F. Merlin et al. 2017; N. Pinilla-Alonso et al. 2025).

The visible reflectance spectra of ices combining methane with ammonia, carbon monoxide, carbon dioxide, and methanol (Ices 17–24) exhibit noticeable reddening during the irradiation (Figures 4(e)–(f) and 6(a)–(f)). For the methane–ammonia ice mixture at 20 K, the color slope grows to 18% per 100 nm from 6% per 100 nm, and at 10 K, 25% per 100 nm from about zero in the approximately exponential growth

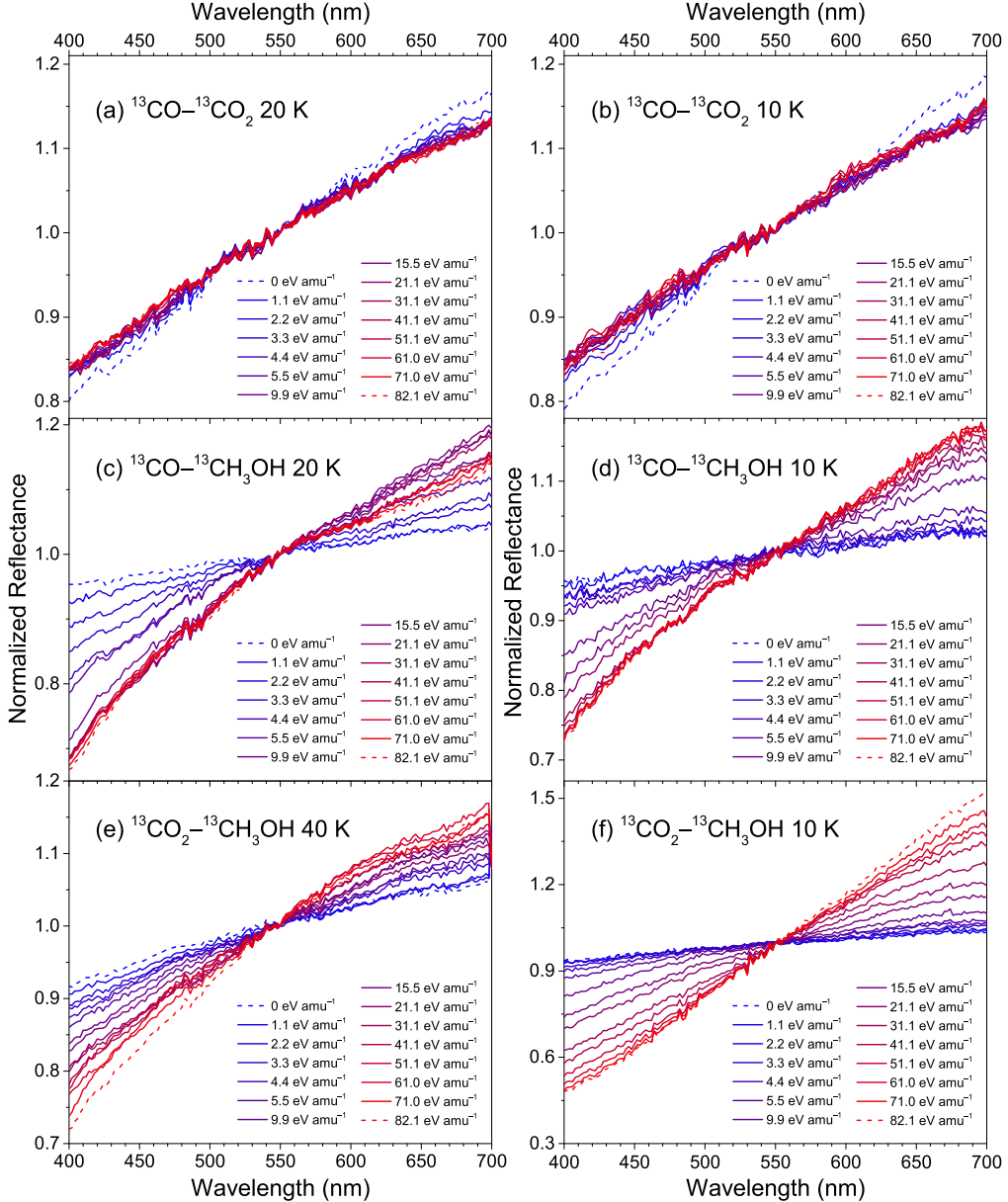


Figure 9. The visible reflectance spectra of ices 31–36 measured during the irradiation. Ices 31–36 in Table 1 are displayed in the order of (a)–(f). All spectra are normalized at 550 nm and plotted as a gradient color from blue to red as radiation dose increases. Dashed lines represent the spectra of ices before and after irradiation.

(Figure 5(e)). The slopes of methane–carbon monoxide ices at 20 and 10 K exhibit similar increase profiles at the high-dose region with final color slopes of 23% per 100 nm and 19% per 100 nm (Figure 5(g)). In the low-dose region, the slopes at 10 K first rise quickly and then decrease slightly. This may be due to the fast growth of color slopes from processed carbon monoxide at 10 K (C. Zhang et al. 2024). The color slopes of methane–carbon dioxide ice mixtures at 20 K initially go down slightly and then go up to an asymptotic value of about 13% per 100 nm (Figure 5(i)). At 10 K, their color slopes decrease from 7% per 100 nm to 3% per 100 nm before the dose of 5 eV amu⁻¹ and later increase to 32% per 100 nm (Figure 5(i)). The color slopes of irradiated methane–methanol ice mixtures at both temperatures increase with approximately linear growth and overlap in the high-dose region with a final value of 19% per 100 nm at 20 K and 20% per 100 nm at 10 K (Figure 5(k)). The $B - V$ colors of these ice mixtures are in the range of 0.65–1.05 and the $V - R$ colors are in the range of 0.35–0.66

(Figures 5(f), (h), (j), and (l)). The $V - R$ colors of irradiated ices of methane mixed with ammonia, carbon monoxide, and methanol are lower than those of TNOs’ observations (Figures 5(f), (h), and (l)). The colors of irradiated methane–carbon dioxide at 10 K (Figure 5(j)) replicate that of red matter on some TNOs such as 50000 Quaoar (M. A. Barucci et al. 2005; M. A. Barucci et al. 2011).

The visible reflectance spectra of ammonia mixed with carbon monoxide, carbon dioxide, and methanol (Ices 25–30) present reddening at different levels during the irradiation (Figures 7(a)–(f)). Their color slopes and colors are included in Figure 8. The color slopes of processed ammonia–carbon monoxide ice mixtures increase at both temperatures with the final values of 10% per 100 nm at 20 K and 30% per 100 nm at 10 K (Figure 8(a)). Note that although this system exhibits reddening at 10 K, it is still lower than processed pure carbon monoxide at the same temperature (C. Zhang et al. 2024). At 20 K, the colors of this system mainly occupy the range of

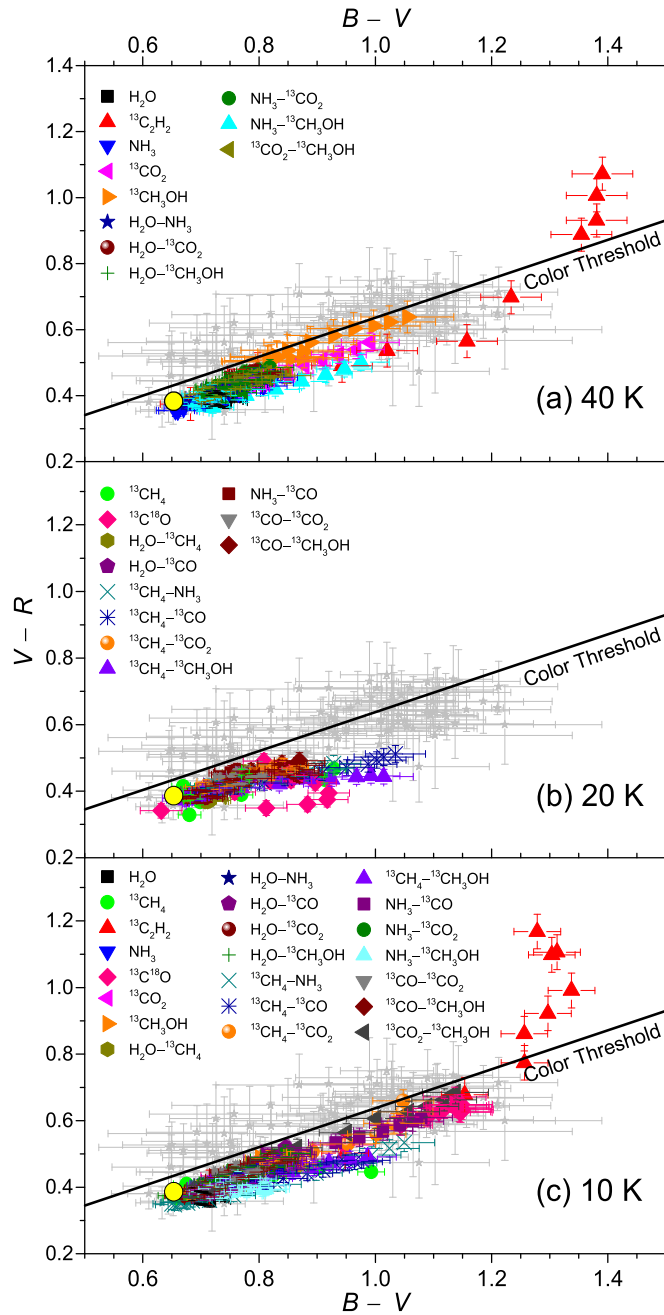


Figure 10. Colors obtained at different temperatures of (a) 40 K, (b) 20 K, and (c) 10 K. The color of the Sun is labeled with a yellow circle. The gray area is the colors of TNOs from observations (O. R. Hainaut et al. 2012). The colors of methane ($^{13}\text{CH}_4$), acetylene ($^{13}\text{C}_2\text{H}_2$), methanol ($^{13}\text{CH}_3\text{OH}$), and carbon monoxide (^{13}CO) ices are from previous publications (C. Zhang et al. 2023; C. Zhang et al. 2024). A color threshold is plotted to divide the observed data covered by the colors obtained in laboratory ices from what is uncovered.

$B - V \approx 0.69$ to 0.76 and $V - R \approx 0.38$ to 0.45 (Figure 8(b)), and overlap that of some neutral TNOs. At 10 K, the colors fall within the range of $B - V \approx 0.69$ – 1.08 and $V - R \approx 0.37$ – 0.61 (Figure 8(b)), which can match parts of the very red TNOs, such as (119951) 2002 KX₁₄ (O. R. Hainaut et al. 2012). For ammonia–carbon dioxide ice mixtures, the color slopes first decrease, followed by a slow increase (Figure 8(c)). After irradiation, the color slopes are 12% per 100 nm at 40 K and 16% per 100 nm at 10 K. The colors of this system are mainly located in the neutral region defined by $B - V \approx 0.72$ to 0.85

and $V - R \approx 0.41$ to 0.50 (Figure 8(d)). The color slopes of ammonia–methanol ice mixtures have similar evolution patterns of irradiated pure methanol (C. Zhang et al. 2024), but with lower final values of 20% per 100 nm at 40 K and 10% per 100 nm at 10 K (Figure 8(e)). The colors of ammonia–methanol ices processed in low doses reproduce those of some neutral TNOs (Figure 8(f)), such as (24952) 1997 QJ₄ (O. R. Hainaut et al. 2012). The $V - R$ colors in the high doses are lower than those of TNOs (Figure 8(f)).

It is surprising that the reflectance spectra of carbon monoxide–carbon dioxide ice mixtures only exhibit slightly negative shifts (Ices 31 and 32, Figures 9(a) and (b)). Their color slopes are from about 12% to 10% per 100 nm as the radiation dose is extended (Figure 8(g)) and their colors are in a small area of $B - V \approx 0.76$ – 0.81 and $V - R \approx 0.45$ – 0.47 (Figure 8(h)). This finding suggests the addition of carbon dioxide can prevent the reddening reactions in carbon monoxide ices (C. Zhang et al. 2024). The reflectance spectra of carbon monoxide–methanol ices show reddening behaviors during the irradiation (Ices 33 and 34, Figures 9(c) and (d)). Their color slopes climb to 14% per 100 nm at both temperatures but increase faster at 20 K (Figure 8(i)). The colors of this ice mixture are located in the neutral region within 0.68– 0.87 for $B - V$ values and 0.38– 0.49 for $V - R$ (Figure 8(j)). For the spectra of processed carbon dioxide–methanol ice mixtures (Ices 35 and 36, Figures 9(e) and (f)), their color slopes rise to 14% per 100 nm at 40 K and increase to 36% per 100 nm at 10 K (Figure 8(k)), which reveals a significant influence of irradiation temperature. At 40 K, colors occupy the neutral position defined by $B - V \approx 0.70$ – 0.85 and $V - R \approx 0.39$ – 0.46 . At 10 K, $B - V$ and $V - R$ colors are in the range of 0.68– 1.14 and 0.39– 0.68 (Figure 8(l)), and the final value is very close to that of the ultrared surface of TNOs, for example, Sedna (O. R. Hainaut et al. 2012).

3.3. Temperature Effect

The colors of all ices during irradiation are gathered in the color–color diagram (Figure 10). It is found that the colors of processed laboratory ice analogs can cover most neutral parts and some of the ultrared parts of TNOs and leave a part of uncovered data. We divide the covered and uncovered data using a color threshold line. The failure to reproduce the TNO colors above the color threshold indicates that molecular carriers with low-lying electronic transitions (N. J. Turro 1991) are unaccounted for, e.g., possibly processed hydrogen sulfide ices and silicates that have been tentatively detected on TNOs and can produce sulfur-bearing polymers and metallic iron (B. Hapke 2001; A. Mahjoub et al. 2017; M. J. Poston et al. 2018; T. Seccull et al. 2018). Water-rich ices have similar values after irradiation and are independent of the irradiation temperature (Figures 2 and 5). Pure ammonia decreases in color slopes during irradiation and can also reduce the reddening of other ices in the ammonia-bearing ice mixtures (Figure 8). Interestingly, carbon dioxide can significantly enhance the reddening of methane and methanol at 10 K (Figures 5(i) and 8(k)), but carbon dioxide itself does not show significant changes in colors at this temperature (Figure 2(f)). This finding suggests that some of the products from irradiated carbon dioxide can promote the reactions in methane and methanol ices to produce ultrared matter, such as the suprathermal oxygen atoms (C. S. Jamieson et al. 2006). More importantly, some ice mixtures, such as carbon dioxide and methanol,

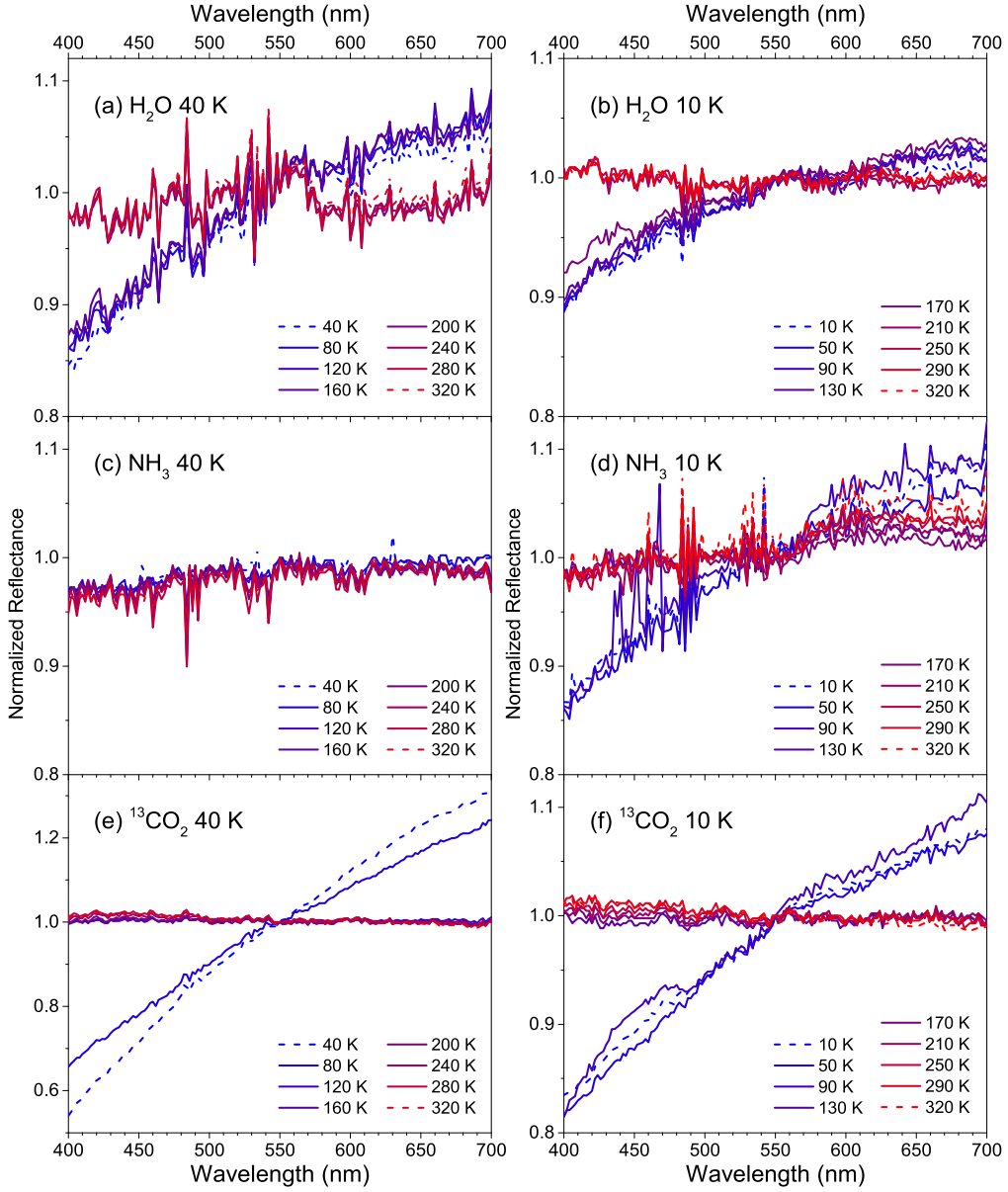


Figure 11. The visible reflectance spectra of irradiated ices 1–6 taken during heating to 320 K. Ices 1–6 in Table 1 are displayed in the order of (a)–(f). All spectra are normalized at 550 nm and plotted as a gradient color from blue to red as temperature increases. Dashed lines represent the spectra of irradiated ices before and after heating to 320 K.

exhibit distinct colors when exposed to different irradiation temperatures. These results indicate that the wide range of colors observed from TNOs can be attributed not only to varying levels of irradiation affecting their surface compositions but also to the same initial compounds experiencing irradiation at different temperatures.

In order to study the thermal stability of colors from irradiated TNO ice analogs, we also collect their visible reflectance spectra during heating to 320 K (Figures 11–16) and gather the color slopes in Figure 17. This evolution is strongly relevant to the missing ultrared materials of Jupiter-family comets, whose surface temperature can reach about 150 K (S. S. Sheppard 2010; C. J. Bennett et al. 2013; D. Jewitt 2015). These bodies supposedly originated in trans-Neptunian space and the surface materials are possibly sublimated or destroyed when transferred into the inner solar system (S. S. Sheppard 2010; C. J. Bennett et al. 2013;

A. Morbidelli & D. Nesvorný 2020). The color slopes of irradiated pure water, ammonia, and carbon dioxide decrease to nearly zero as the molecular ice sublimes (Figures 11, 17(a) and (b)), which suggests that corresponding products are unstable and easily desorb as temperature increases. This is different from the residues of irradiated methane, carbon monoxide, and methanol, whose color slopes stay thermally stable during heating to 320 K (C. Zhang et al. 2023; C. Zhang et al. 2024). For water-containing irradiated ices, water–ammonia and water–carbon dioxide ice mixtures decrease to nearly zero on color slopes as water molecules are released, the color slopes of irradiated water–methane ices show temperature independence during heating to 320 K, and the water–carbon monoxide sample’s color slopes are stable before water sublimates but present an oscillation at high temperatures; irradiated water–methanol is also stable before water release but increases after water sublimates, followed by a decrease

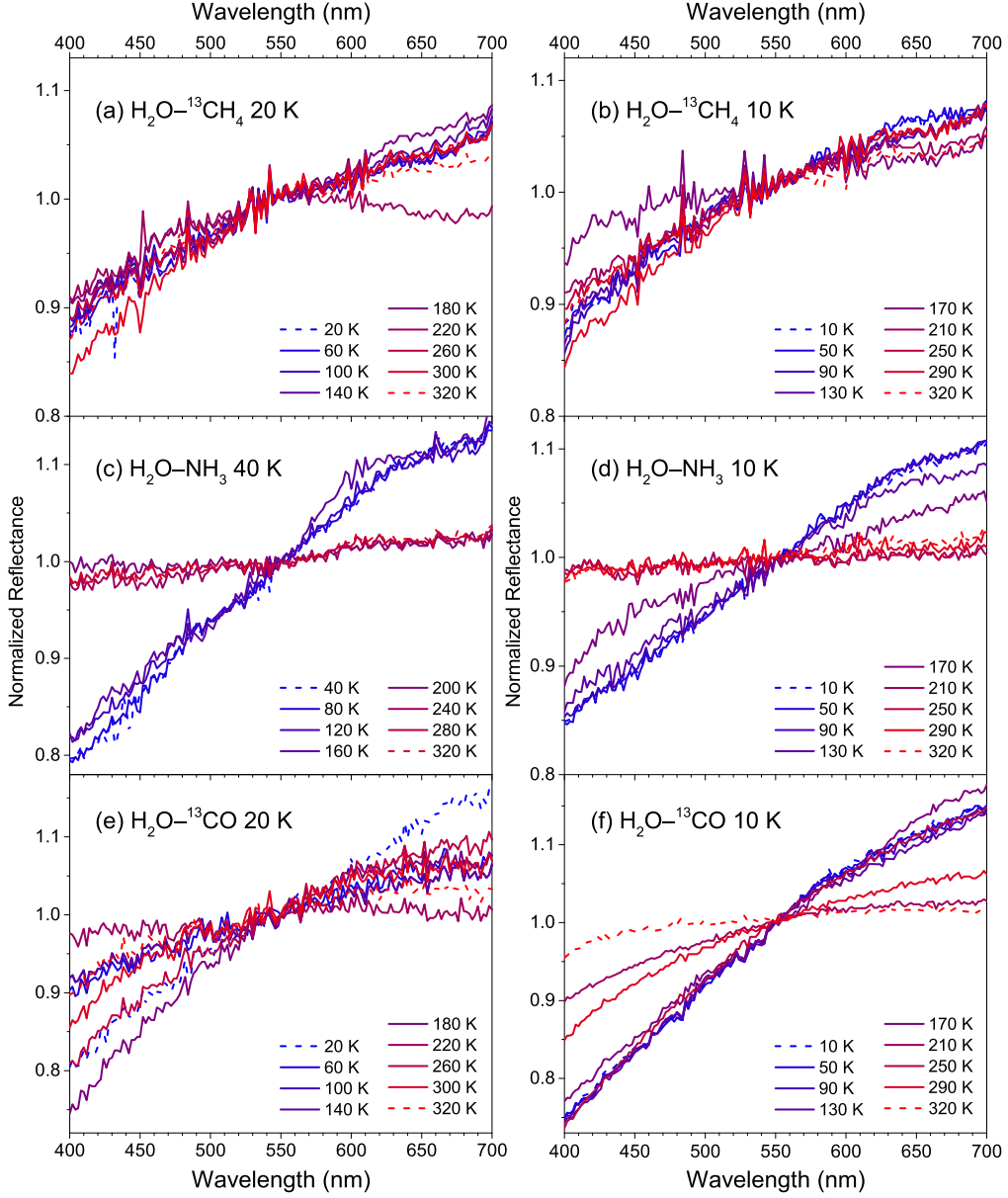


Figure 12. The visible reflectance spectra of irradiated ices 7–12 taken during heating to 320 K. Ices 7–12 in Table 1 are displayed in the order of (a)–(f). All spectra are normalized at 550 nm and plotted as a gradient color from blue to red as temperature increases. Dashed lines represent the spectra of irradiated ices before and after heating to 320 K.

due to the desorption of products having high color slopes (Figures 12, 13(a)–(d), 17(a)–(d)). For methane-bearing ices, the color slopes of irradiated methane–ammonia and methane–methanol ices only decrease slightly during heating to 320 K, the color slopes of methane–carbon monoxide ice mixtures show no alteration with increasing temperature, and those of a methane–carbon dioxide system decrease before 130 K and then present vibration during heating to 320 K (Figures 13(e) and (f), 14, 17(c) and (d)). Except for the ammonia–methanol mixture irradiated at 10 K, which exhibits some increase in color slopes at 320 K, the color slopes of other ice mixtures (ices 25–36) decrease at varying levels (Figures 15, 16, 17(e) and (f)) during heating to 320 K. It is noteworthy that nonlinear reflectance, which increases in various degrees, is observed when heating some of the irradiated ice mixtures, such as the spectrum at 220 K of the $^{13}\text{CH}_4-\text{NH}_3$ ices irradiated at 20 K, and the spectrum at 320 K of the $^{13}\text{CH}_4-\text{CH}_3\text{OH}$ ices

irradiated at both temperatures. These features with higher spectral slopes at shorter wavelengths and flattening slopes at longer wavelengths may be attributed to Rayleigh scattering caused by the grain-size materials formed during heating of the irradiated ices, which has been reported in the visible and near-infrared spectra of small bodies located in the inner solar system, for example, Jupiter Trojans (J. P. Emery & R. H. Brown 2004; J. P. Emery et al. 2011; R. N. Clark et al. 2012; A. J. Brown 2014; A. C. Souza-Feliciano et al. 2020; O. A. Humes et al. 2022; O. A. Humes et al. 2024). In addition, during heating to 320 K, not only does the temperature-dependent refractive index of ice affect its reflectance, but the reactants and unstable products can also sublime and abruptly alter the thickness and porosity of the ice. These sudden changes probably result in biased visible reflectance spectra such as large variations in color slopes, especially in the high-temperature region. Altogether, the color

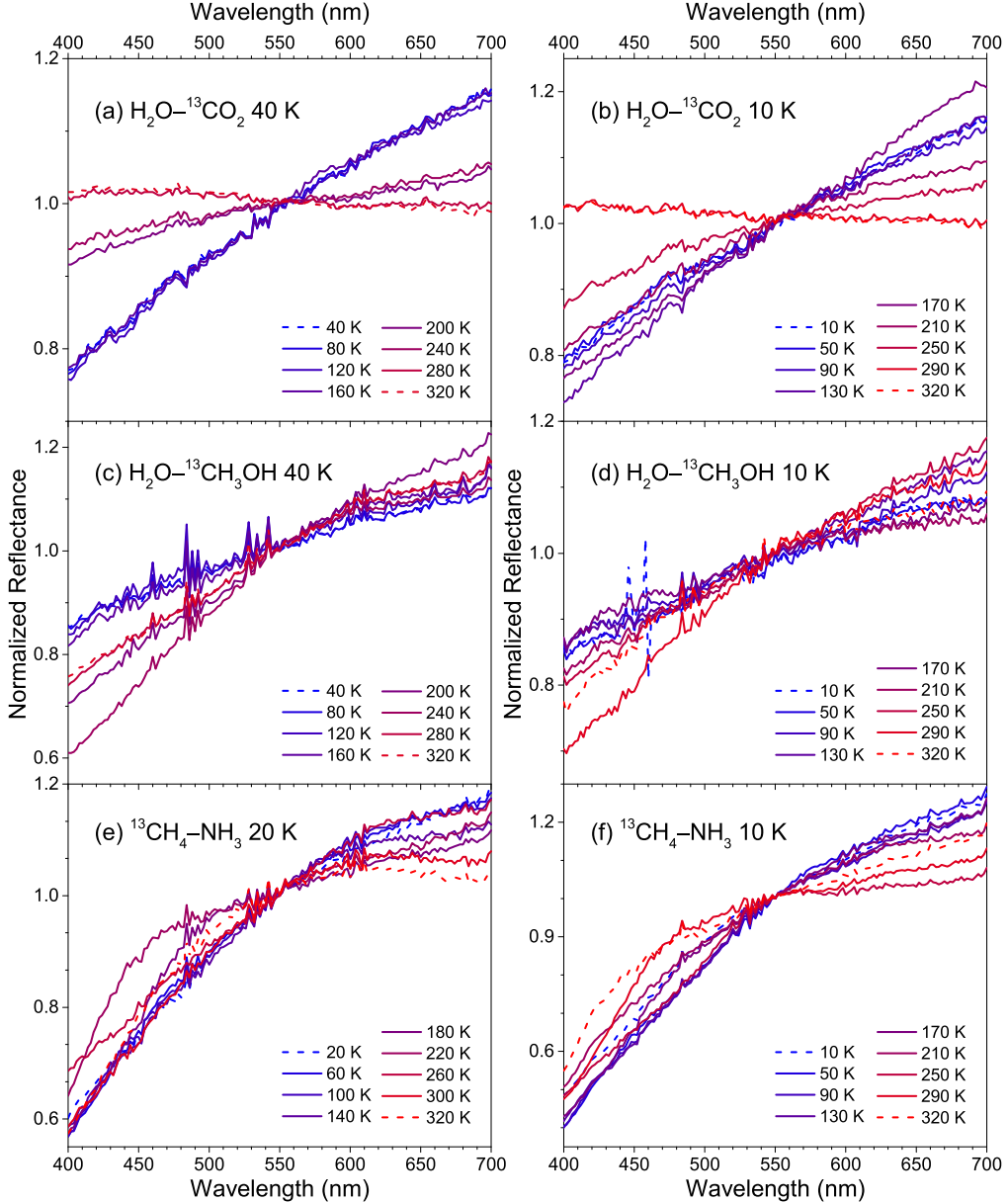


Figure 13. The visible reflectance spectra of irradiated ices 13–18 taken during heating to 320 K. Ices 13–18 in Table 1 are displayed in the order of (a)–(f). All spectra are normalized at 550 nm and plotted as a gradient color from blue to red as temperature increases. Dashed lines represent the spectra of irradiated ices before and after heating to 320 K.

slopes of all ices are thermally stable without much change before the release of reactants; thereafter, they present variable behavior, possibly due to the alteration of thickness, cosublimation of high-color-slope products with reactants, or the formation of macromolecules triggered by thermal reactions.

4. Conclusions and Astrophysical Implications

This work presents the evolution of visible reflectance, spectral slopes, and colors of TNO-related ices exposed to ionizing radiation. These experiments aim to study how the initial composition, radiation dose, and processing temperature affect the observed color diversity of TNOs, which is important in understanding their surface compositions, as well as their formation and migration. First, the current and previous data provide compelling evidence that ionizing-radiation exposure on frozen molecules of methane, carbon monoxide, carbon

dioxide, and methanol, along with acetylene, can significantly redden their visible reflectance spectra due to the formation of complex organic molecules (C. Zhang et al. 2023; C. Zhang et al. 2024), which contain delocalized electrons and can absorb light of various visible wavelengths. The spectral slopes of irradiated water ices are neutral and independent of the radiation dose, whereas those of ammonia decrease as the radiation dose accumulates. Second, the addition of water and ammonia in ice mixtures can reduce the color slopes compared to corresponding pure ices, which indicates that water- and ammonia-rich small TNOs are more likely to be defined as neutral TNOs. Third, we demonstrate that the irradiation temperature can control the reddening processes of ices containing carbon and oxygen, in that the color slopes of methanol and carbon dioxide ices increase when irradiated at 40 K but there is almost no change at 10 K, whereas processed

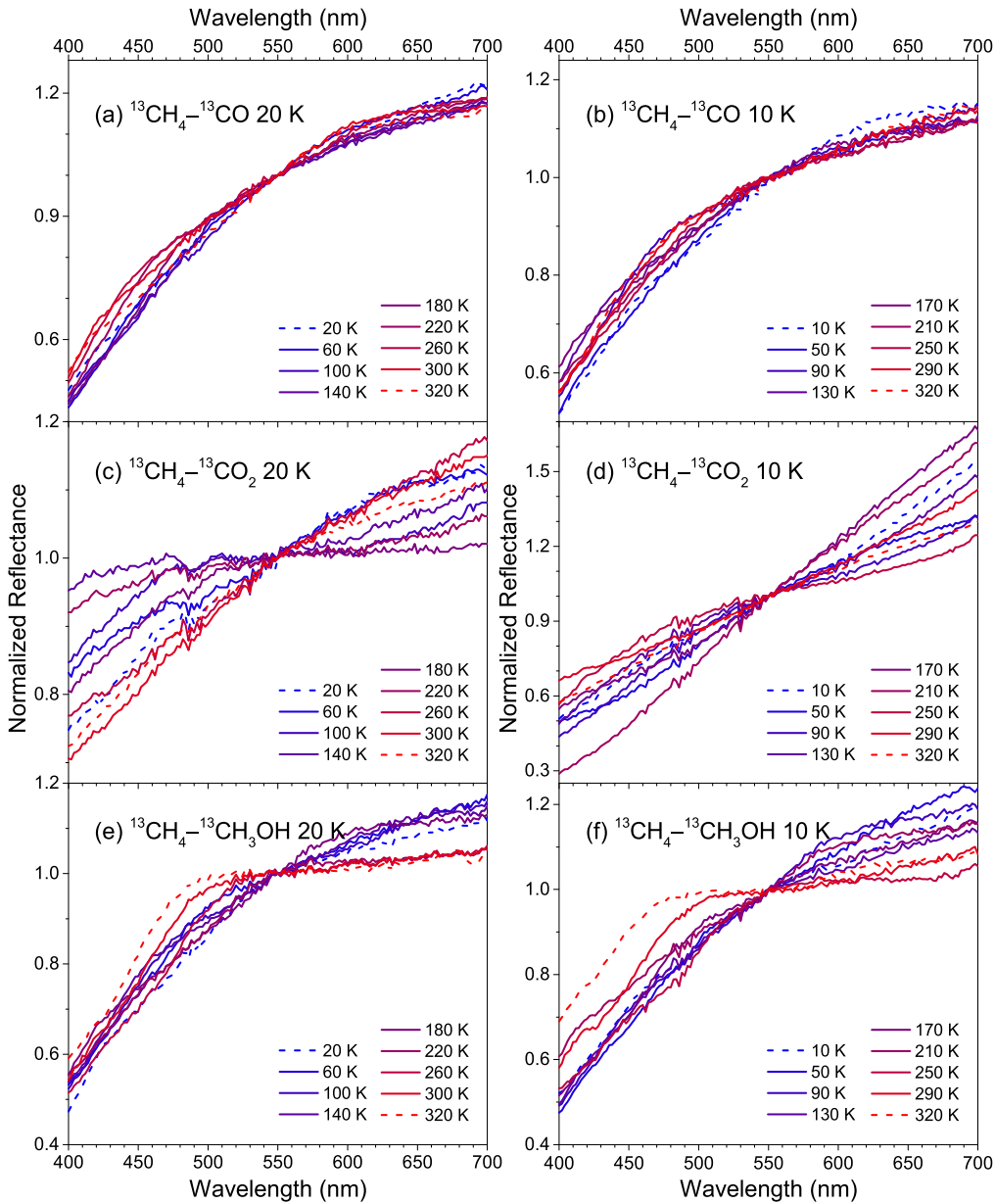


Figure 14. The visible reflectance spectra of irradiated ices 19–24 taken during heating to 320 K. Ices 19–24 in Table 1 are displayed in the order of (a)–(f). All spectra are normalized at 550 nm and plotted as a gradient color from blue to red as temperature increases. Dashed lines represent the spectra of irradiated ices before and after heating to 320 K.

carbon dioxide–methanol ice mixtures at 10 K can be classified as ultrared materials with a color slope of 36% per 100 nm but only increase to 14% per 100 nm at 40 K. However, there is no evidence of a correlation between the evolution of color slopes and irradiated temperature for hydrocarbon molecules such as methane and acetylene (C. Zhang et al. 2023). Finally, during heating to 320 K, the color slopes of irradiated methane and acetylene present as temperature independent; methanol, carbon monoxide, methane–ammonia, methane–carbon monoxide, and methane–methanol show slight reductions. The color slopes of the rest of the ices are stable before the reactants release out but become unstable in the high-temperature region, which might be due to the products cosublimating with the reactants, or the formation of complex macromolecules.

These results suggest that the surface color of TNOs could be representative of their surface compositions to some degree and provide important laboratory data for the modeling of TNO

photometric observations, such as the Hale Telescope and New Horizons (J. Luu & D. Jewitt 1996a; C. M. Dalle Ore et al. 2013; F. Merlin et al. 2017; R. E. Pike et al. 2017; I. Wong et al. 2019; M. A. Barucci & F. Merlin 2020; W. M. Grundy et al. 2020; J. D. Hofgartner et al. 2021). The visible spectra of residues from irradiated ices, combined with infrared spectra, are also important for explaining compositions on TNOs, for example, the complex organics observed by JWST on Sedna, Gonggong, and Quaoar (J. P. Emery et al. 2024). The estimated time for the radiation dose reaching 1 eV amu^{-1} at a TNO surface of 100 nm is about $2.4 \times 10^7 \text{ yr}$ (J. F. Cooper et al. 2003; M. J. Loeffler et al. 2020; E. Quirico et al. 2023). Therefore, the radiation dose used here mimics the GCR exposure on a TNO surface for an equivalent of approximately 1800 million years. This work represents a thorough investigation of how the original surface species and chemical reactions along with temperature influence the observed colors

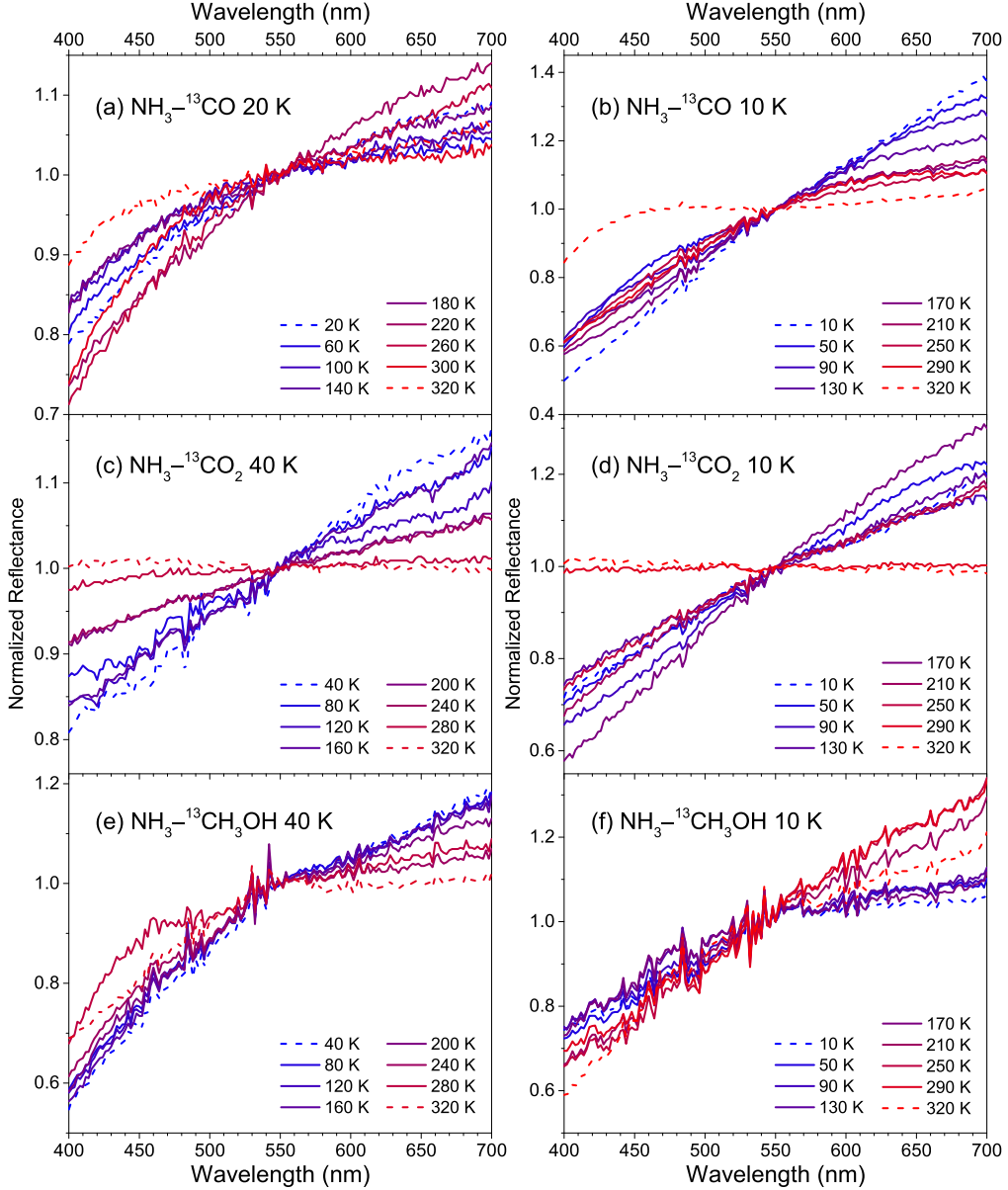


Figure 15. The visible reflectance spectra of irradiated ices 25–30 taken during heating to 320 K. Ices 25–30 in Table 1 are displayed in the order of (a)–(f). All spectra are normalized at 550 nm and plotted as a gradient color from blue to red as temperature increases. Dashed lines represent the spectra of irradiated ices before and after heating to 320 K.

of TNOs. It can also serve as a probe for understanding the history and current levels of radiation processes in small objects within the outer solar system (C. M. Dalle Ore et al. 2011; R. I. Kaiser et al. 2011). The visible reflectance spectra present here can help to obtain key parameters such as the wavelength-dependent refractive index for radiative transfer modeling (S. Li & L. Li 2011; B. Hapke 2012; J. K. Harris & P. M. Grindrod 2018), and afford the potential to inventory complex organic molecules synthesized in the trans-Neptunian space (C. J. Bennett et al. 2013; A. Potapov et al. 2020; R. Martinez et al. 2022). The decrease of color slopes for some irradiated ices during heating to 320 K is strongly relevant to the missing ultrared materials of small bodies closer to the Sun than TNOs, such as centaurs and Jupiter-family comets (D. C. Jewitt 2002; W. M. Grundy 2009; J. Licandro et al. 2025).

The current study provides the most comprehensive visible reflectance evolution of TNO-analog ices under a low-temperature ionizing-radiation environment as well as heating processing. However, the possible detection of hydrogen sulfide and silicates at some TNOs has also been reported (J. R. Brucato et al. 2003; T. Seccull et al. 2018; A. Mahjoub et al. 2021; T. Seccull et al. 2024). The ionizing-radiation exposure to hydrogen sulfide ices can lead to the formation of sulfur-bearing polymer products, which exhibit strong absorptions in the visible wavelength range (B. Meyer 1976; Y. J. Chen et al. 2014; A. Mahjoub et al. 2017; M. J. Poston et al. 2018). Upon space weathering, the silicates present significant darkening and reddening in the visible and near-infrared spectra due to the formation of metallic iron or structural modifications (C. J. Bennett et al. 2013; R. Brunetto et al. 2015; S. Rubino et al. 2024). The addition of hydrogen sulfide and silicates in the TNO ice analogs would partially

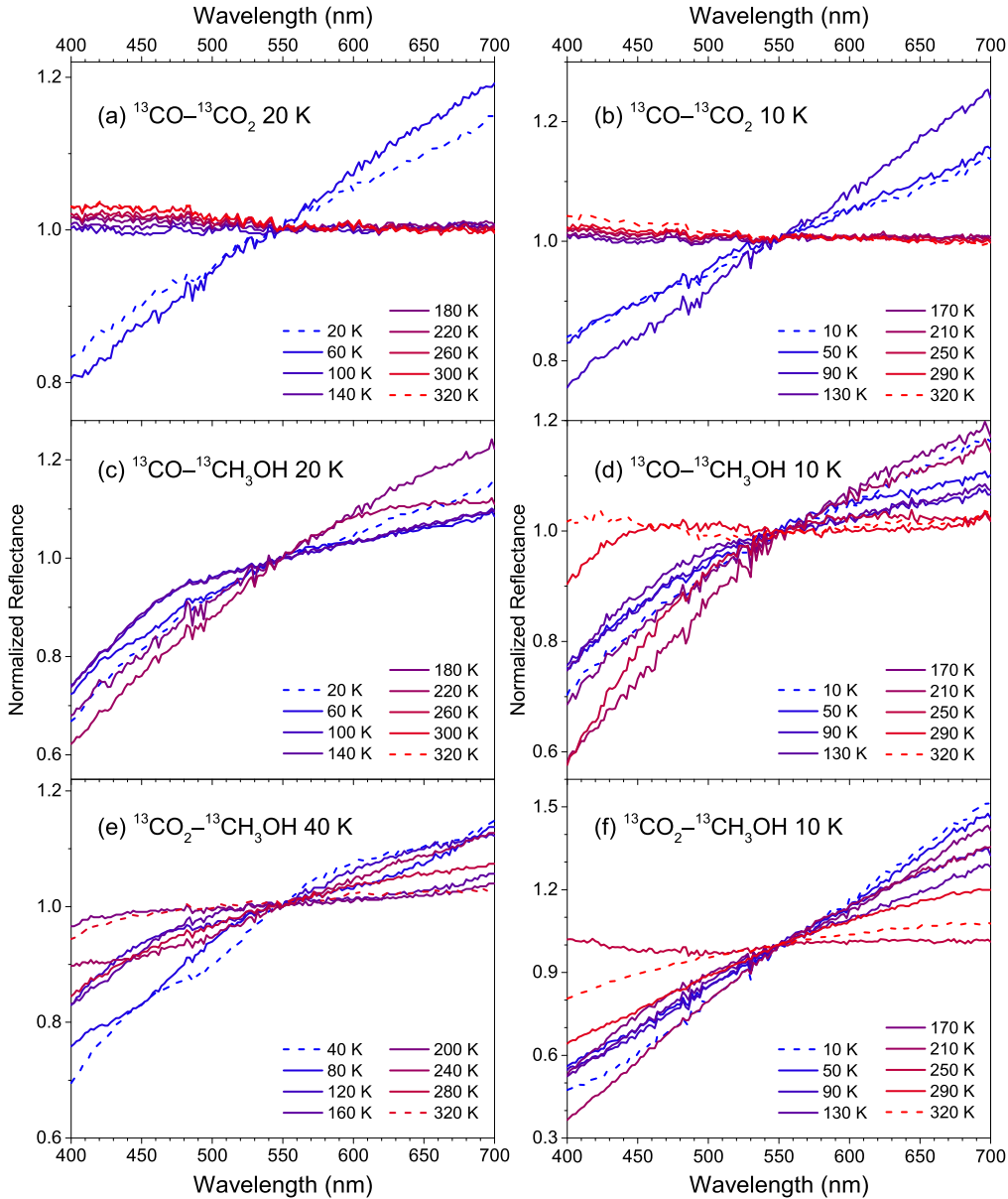


Figure 16. The visible reflectance spectra of irradiated ices 31–36 taken during heating to 320 K. Ices 31–36 in Table 1 are displayed in the order of (a)–(f). All spectra are normalized at 550 nm and plotted as a gradient color from blue to red as temperature increases. Dashed lines represent the spectra of irradiated ices before and after heating to 320 K.

increase the average spectral slopes during irradiation. Therefore, further experiments are warranted to probe ices mixed with hydrogen sulfide and silicates to gauge their spectral characteristics in the visible region, which is also important for interpreting photometric observations of asteroids located in the inner solar system (L. Galluccio et al. 2023). On the other hand, the present laboratory experiments only simulate ionizing radiation and thermal processing for the surface icy mantle of airless TNOs and neglect the color modification from dynamical processes such as randomized collisional excavation, velocity-dependent impact resurfacing, fall-back debris condensation from comet-like activity, and seasonal transport of volatile molecules (J. Luu & D. Jewitt 1996a; S. A. Stern 2002; A. Doressoundiram et al. 2008; C. J. Bennett et al. 2013; B. J. Buratti et al. 2015; T. Bertrand & F. Forget 2016; W. M. Grundy et al. 2016; F. Forget et al. 2017; T. Bertrand et al. 2018; T. Bertrand et al. 2019; N. Bouziani & D. Jewitt 2022; H. A. Ballantyne et al. 2024;

A. Doner et al. 2024), which tend to counteract the reddening alteration from irradiation and require further investigations (J. Luu & D. Jewitt 1996b; L. E. Buchanan et al. 2022; E. Quirico et al. 2023). In addition, some high color slopes from visible reflectance spectra of processed ices suggest that complex organic molecules containing conjugated π -bond systems (R. B. Woodward 1941; L. F. Fieser et al. 1948) are possibly widespread in the trans-Neptunian space, but it is not feasible to define specific chromophores—functional groups responsible for their colors—from the visible reflectance spectra due to the lack of distinctive features. To further explore the physical and chemical properties of TNO surface compounds, complementary analytical techniques including infrared spectroscopy, mass spectrometry, and gas chromatography are also required; in particular, near/mid-infrared spectra can provide fundamental support to explain observations from JWST (M. K. McClure et al. 2023; N. G. C. Brunken et al. 2024; J. P. Emery et al. 2024; M. N. De Prá et al. 2025;

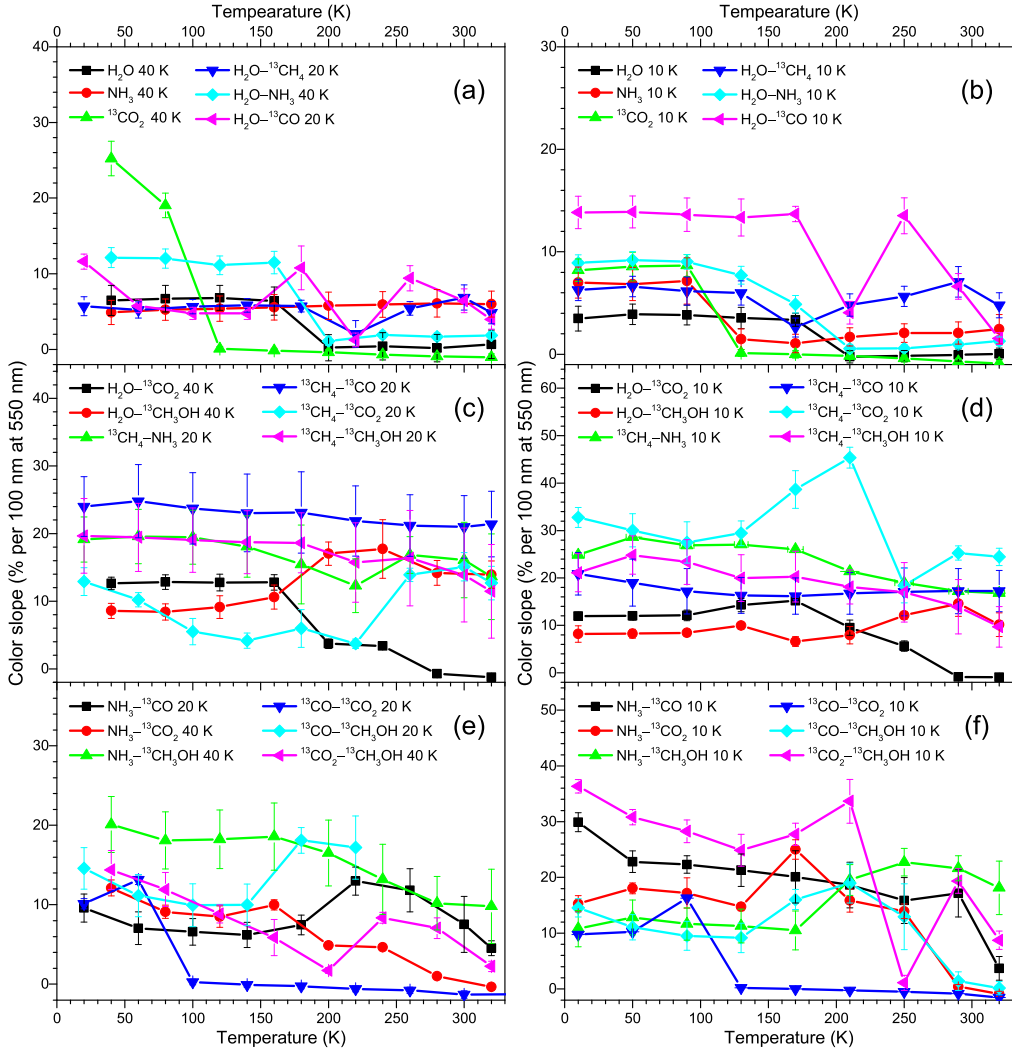


Figure 17. The color slope evolution of irradiated ices taken during heating to 320 K, sequenced in panels (a)–(f). Error bars shown are from the linear fitting of reflectance spectra.

N. Pinilla-Alonso et al. 2025). These synergistic research techniques are expected to develop the concept of how complex molecules were synthesized in the outer solar system, ultimately leading to a better understanding of the origin and evolution of our solar system.

Acknowledgments

We thank the anonymous referee for the valuable comments on the manuscript. This study was supported by the U.S. National Aeronautics and Space Administration (NASA) under grant No. 80NSSC21K1834.

ORCID iDs

Chaojiang Zhang <https://orcid.org/0000-0003-3727-901X>
 Jia Wang <https://orcid.org/0000-0002-3795-8699>
 Leslie A. Young <https://orcid.org/0000-0002-7547-3967>
 Ralf I. Kaiser <https://orcid.org/0000-0002-7233-7206>

References

- Abplanalp, M. J., Jones, B. M., & Kaiser, R. I. 2018, *PCCP*, 20, 5435
 Altweig, K., Balsiger, H., Bar-Nun, A., et al. 2016, *SciA*, 2, e1600285

- Arumainayagam, C. R., Garrod, R. T., Boyer, M. C., et al. 2019, *ChSRv*, 48, 2293
 Augé, B., Dartois, E., Engrand, C., et al. 2016, *A&A*, 592, A99
 Ballantyne, H. A., Asphaug, E., Denton, C. A., Emsenhuber, A., & Jutzi, M. 2024, *NatAs*, 8, 748
 Baratta, G. A., Leto, G., & Palumbo, M. E. 2002, *A&A*, 384, 343
 Barucci, M. A., Alvarez-Candal, A., Merlin, F., et al. 2011, *Icar*, 214, 297
 Barucci, M. A., Belskaya, I. N., Fulchignoni, M., & Burlan, M. 2005, *AJ*, 130, 1291
 Barucci, M. A., Boehnhardt, H., Cruikshank, D. P., & Morbidelli, A. 2008a, in *The Solar System Beyond Neptune*, ed. M. A. Barucci (1st ed.; Tucson, AZ: Univ. Arizona Press)
 Barucci, M. A., Brown, M., Emery, J., & Merlin, F. 2008b, in *The Solar System Beyond Neptune*, ed. M. A. Barucci et al. (1st ed.; Tucson, AZ: Univ. Arizona Press), 143
 Barucci, M. A., & Merlin, F. 2020, in *The Trans-Neptunian Solar System*, ed. D. Prialnik et al. (1st ed; Amsterdam: Elsevier Science), 109
 Barucci, M. A., Merlin, F., Guilbert, A., et al. 2008c, *A&A*, 479, L13
 Bennett, C. J., Jamieson, C., Mebel, A. M., & Kaiser, R. I. 2004, *PCCP*, 6, 735
 Bennett, C. J., Jamieson, C. S., Osamura, Y., & Kaiser, R. I. 2005, *ApJ*, 624, 1097
 Bennett, C. J., Jamieson, C. S., Osamura, Y., & Kaiser, R. I. 2006, *ApJ*, 653, 792
 Bennett, C. J., Pirim, C., & Orlando, T. M. 2013, *ChRv*, 113, 9086
 Bertrand, T., & Forget, F. 2016, *Natur*, 540, 86
 Bertrand, T., Forget, F., Umurhan, O. M., et al. 2018, *Icar*, 309, 277
 Bertrand, T., Forget, F., Umurhan, O. M., et al. 2019, *Icar*, 329, 148
 Bouilloud, M., Fray, N., Bénilan, Y., et al. 2015, *MNRAS*, 451, 2145

- Bouziani, N., & Jewitt, D. 2022, *ApJ*, **924**, 37
- Brown, A. J. 2014, *Icar*, **239**, 85
- Brown, M. E. 2012, *AREPS*, **40**, 467
- Brown, M. E., & Fraser, W. C. 2023, *PSJ*, **4**, 130
- Brown, M. E., Schaller, E. L., & Fraser, W. C. 2011, *ApJL*, **739**, L60
- Brown, M. E., Schaller, E. L., & Fraser, W. C. 2012, *AJ*, **143**, 146
- Brucato, J. R., Strazzulla, G., Baratta, G., Mennella, V., & Colangeli, L. 2003, *EM&P*, **92**, 307
- Brunetto, R., Barucci, M. A., Dotto, E., & Strazzulla, G. 2006, *ApJ*, **644**, 646
- Brunetto, R., Loeffler, M. J., Nesvorný, D., Sasaki, S., & Strazzulla, G. 2015, in Asteroids, ed. P. Michel et al. (Tucson, AZ: Univ. Arizona Press), 597
- Brunkent, N. G. C., Rocha, W. R. M., van Dishoeck, E. F., et al. 2024, *A&A*, **685**, A27
- Buchanan, L. E., Schwamb, M. E., Fraser, W. C., et al. 2022, *PSJ*, **3**, 9
- Buratti, B. J., Hicks, M. D., Dalba, P. A., et al. 2015, *ApJL*, **804**, L6
- Chen, Y. J., Jiang, K. J., Nuevo, M., et al. 2014, *ApJ*, **798**, 80
- Chyba, C., & Sagan, C. 1992, *Natur*, **355**, 125
- Chyba, C. F., Thomas, P. J., Brookshaw, L., & Sagan, C. 1990, *Sci*, **249**, 366
- Clark, R. N., Cruikshank, D. P., Jaumann, R., et al. 2012, *Icar*, **218**, 831
- Coelho, L. F., Madden, J., Kaltenegger, L., et al. 2022, *AsBio*, **22**, 313
- Cook, J. C., Protopapa, S., Dalle Ore, C. M., et al. 2023, *Icar*, **389**, 115242
- Cooper, G., Kimmich, N., Belisle, W., et al. 2001, *Natur*, **414**, 879
- Cooper, G., & Rios, A. C. 2016, *PNAS*, **113**, E3322
- Cooper, J. F., Christian, E. R., Richardson, J. D., & Wang, C. 2003, *EM&P*, **92**, 261
- Cronin, J. R., & Pizzarelli, S. 1997, *Sci*, **275**, 951
- Cruikshank, D. P., Grundy, W. M., DeMeo, F. E., et al. 2015, *Icar*, **246**, 82
- Cruikshank, D. P., Imanaka, H., & Dalle Ore, C. M. 2005, *AdSpR*, **36**, 178
- Cruikshank, D. P., Materese, C. K., Pendleton, Y. J., et al. 2019, *AsBio*, **19**, 831
- Dalle Ore, C. M., Barucci, M. A., Emery, J. P., et al. 2015, *Icar*, **252**, 311
- Dalle Ore, C. M., Dalle Ore, L. V., Roush, T. L., et al. 2013, *Icar*, **222**, 307
- Dalle Ore, C. M., Fulchignoni, M., Cruikshank, D. P., et al. 2011, *A&A*, **533**, A98
- De Prá, M. N., Hénault, E., Pinilla-Alonso, N., et al. 2025, *NatAs*, **9**, 252
- DeMeo, F. E., Dumas, C., Cook, J. C., et al. 2015, *Icar*, **246**, 213
- Doner, A., Horányi, M., Bagenal, F., et al. 2024, *ApJL*, **961**, L38
- Doressoundiram, A., Boehnhardt, H., Tegler, S. C., & Trujillo, C. 2008, in The Solar System Beyond Neptune, ed. M. A. Barucci et al. (1st ed.; Tucson, AZ: Univ. Arizona Press), 91
- Drouin, D., Couture, A. R., Joly, D., et al. 2007, *Scanning*, **29**, 92
- Emery, J. P., & Brown, R. H. 2004, *Icar*, **170**, 131
- Emery, J. P., Burr, D. M., & Cruikshank, D. P. 2011, *AJ*, **141**, 25
- Emery, J. P., Wong, I., Brunetto, R., et al. 2024, *Icar*, **414**, 116017
- Fernández-Valenzuela, E., Pinilla-Alonso, N., Stansberry, J., et al. 2021, *PSJ*, **2**, 10
- Fieser, L. F., Fieser, M., & Rajagopalan, S. 1948, *J. Org. Chem.*, **13**, 800
- Forget, F., Bertrand, T., Vangvichith, M., et al. 2017, *Icar*, **287**, 54
- Fornasier, S., Barucci, M. A., de Bergh, C., et al. 2009, *A&A*, **508**, 457
- Forstel, M., Maksyutenko, P., Jones, B. M., et al. 2016, *ChCom*, **52**, 741
- Fraser, W. C., Benecchi, S. D., Kavelaars, J. J., et al. 2021, *PSJ*, **2**, 90
- Fraser, W. C., & Brown, M. E. 2012, *ApJ*, **749**, 33
- Furukawa, Y., Chikaraishi, Y., Ohkouchi, N., et al. 2019, *PNAS*, **116**, 24440
- Galluccio, L., Delbo, M., De Angeli, F., et al. 2023, *A&A*, **674**, A35
- Gladman, B., & Volk, K. 2021, *ARA&A*, **59**, 203
- Golabek, G. J., & Jutzi, M. 2021, *Icar*, **363**, 114437
- Grundy, W. M. 2009, *Icar*, **199**, 560
- Grundy, W. M., Bird, M. K., Britt, D. T., et al. 2020, *Sci*, **367**, eaay3705
- Grundy, W. M., Cruikshank, D. P., Gladstone, G. R., et al. 2016, *Natur*, **539**, 65
- Hainaut, O. R., Boehnhardt, H., & Protopapa, S. 2012, *A&A*, **546**, A115
- Hapke, B. 2001, *JGR*, **106**, 10039
- Hapke, B. 2012, Theory of Reflectance and Emittance Spectroscopy (2nd ed.; New York: Cambridge Univ. Press)
- Harris, J. K., & Grindrod, P. M. 2018, *M&PS*, **53**, 1179
- He, C., Hörist, S. M., Lewis, N. K., et al. 2018, *ApJL*, **856**, L3
- Heavens, O. S. 1955, Optical Properties of Thin Solid Films (1st ed.; New York: Dover)
- Hofgartner, J. D., Buratti, B. J., Benecchi, S. D., et al. 2021, *Icar*, **356**, 113723
- Holmberg, J., Flynn, C., & Portinari, L. 2006, *MNRAS*, **367**, 449
- Hudson, R., Palumbo, M. E., Strazzulla, G., et al. 2008, in The Solar System Beyond Neptune, ed. M. A. Barucci et al. (1st ed.; Tucson, AZ: Univ. Arizona Press), 507
- Humes, O. A., Thomas, C. A., Emery, J. P., & Grundy, W. M. 2022, *PSJ*, **3**, 190
- Humes, O. A., Thomas, C. A., & McGraw, L. E. 2024, *PSJ*, **5**, 80
- Jamieson, C. S., Mebel, A. M., & Kaiser, R. I. 2006, in AIP Conf. Proc. 855, Astrochemistry: From Laboratory Studies to Astronomical Observations (Melville, NY: AIP), 100
- Jewitt, D. 2015, *AJ*, **150**, 201
- Jewitt, D., & Luu, J. 1993, *Natur*, **362**, 730
- Jewitt, D. C. 2002, *AJ*, **123**, 1039
- Jewitt, D. C., & Luu, J. X. 2001, *AJ*, **122**, 2099
- Johnson, R. E. 1990, Energetic Charged-Particle Interactions with Atmospheres and Surfaces (1st ed.; Berlin: Springer)
- Johnson, R. E. 1991, *JGR*, **96**, 17553
- Jones, B. M., & Kaiser, R. I. 2013, *JPCL*, **4**, 1965
- Kaiser, R. I., Zheng, W., Osamura, Y., & Chang, A. H. 2011, *PCCP*, **13**, 15747
- Kim, Y. S., & Kaiser, R. I. 2012, *ApJ*, **758**, 37
- Kleimeier, N. F., Liu, Y., Turner, A. M., et al. 2022, *PCCP*, **24**, 1424
- Kuan, Y.-J., Charnley, S. B., Huang, H.-C., et al. 2004, *AdSpR*, **33**, 31
- Li, S., & Li, L. 2011, *JGRE*, **116**, E09001
- Licandro, J., Pinilla-Alonso, N., Holler, B. J., et al. 2025, *NatAs*, **9**, 245
- Loeffler, M. J., Tribbett, P. D., Cooper, J. F., & Sturner, S. J. 2020, *Icar*, **351**, 113943
- Luu, J., & Jewitt, D. 1996a, *AJ*, **112**, 2310
- Luu, J., & Jewitt, D. 1996b, *AJ*, **111**, 499
- Luu, J. X., & Jewitt, D. C. 1990, *AJ*, **99**, 1985
- Luu, J. X., & Jewitt, D. C. 2002, *ARA&A*, **40**, 63
- Mahjoub, A., Brown, M. E., Poston, M. J., et al. 2021, *ApJL*, **914**, L31
- Mahjoub, A., Poston, M. J., Blackberg, J., et al. 2017, *ApJ*, **846**, 148
- Martinez, R., Agnihotri, A., da Silveira, E. F., et al. 2022, *Icar*, **375**, 114830
- Materese, C. K., Cruikshank, D. P., Sandford, S. A., Imanaka, H., & Nuevo, M. 2015, *ApJ*, **812**, 150
- Materese, C. K., Cruikshank, D. P., Sandford, S. A., et al. 2014, *ApJ*, **788**, 111
- McClure, M. K., Rocha, W. R. M., Pontoppidan, K. M., et al. 2023, *NatAs*, **7**, 431
- Menten, S. M., Sori, M. M., & Bramson, A. M. 2022, *NatCo*, **13**, 4457
- Merlin, F., Barucci, M. A., de Bergh, C., et al. 2010, *Icar*, **210**, 930
- Merlin, F., Hromakina, T., Perna, D., Hong, M. J., & Alvarez-Candal, A. 2017, *A&A*, **604**, A86
- Meyer, B. 1976, *ChRv*, **76**, 367
- Morbidelli, A., & Nesvorný, D. 2020, in The Trans-Neptunian Solar System, ed. D. Prialnik et al. (1st ed.; Amsterdam: Elsevier), 25
- Muñoz Caro, G. M., Dartois, E., Boduch, P., et al. 2014, *A&A*, **566**, A93
- Nesvorný, D., Li, R., Youdin, A. N., Simon, J. B., & Grundy, W. M. 2019, *NatAs*, **3**, 808
- Nesvorný, D., Vokrouhlický, D., Alexandersen, M., et al. 2020, *AJ*, **160**, 46
- Nesvorný, D., Vokrouhlický, D., Dones, L., et al. 2017, *ApJ*, **845**, 27
- Oba, Y., Takano, Y., Naraoka, H., Watanabe, N., & Kouchi, A. 2019, *NatCo*, **10**, 4413
- Oberg, K. I. 2016, *ChRv*, **116**, 9631
- Oró, J. 1961, *Natur*, **190**, 389
- Pasek, M., & Lauretta, D. 2008, *OLEB*, **38**, 5
- Peixinho, N., Delsanti, A., & Doressoundiram, A. 2015, *A&A*, **577**, A35
- Pike, R. E., Fraser, W. C., Schwamb, M. E., et al. 2017, *AJ*, **154**, 101
- Pinilla-Alonso, N., Brunetto, R., De Prá, M. N., et al. 2025, *NatAs*, **9**, 230
- Pinilla-Alonso, N., Stansberry, J. A., & Holler, B. J. 2020, in The Trans-Neptunian Solar System, ed. D. Prialnik et al. (1st ed.; Amsterdam: Elsevier), 395
- Pinto, O. H., Kelley, M. S. P., Villanueva, G. L., et al. 2023, *PSJ*, **4**, 208
- Poston, M. J., Mahjoub, A., Ehlmann, B. L., et al. 2018, *ApJ*, **856**, 124
- Potapov, A., Bouwman, J., Jäger, C., & Henning, T. 2020, *NatAs*, **5**, 78
- Prasad, S. S., & Tarafdar, S. P. 1983, *ApJ*, **267**, 603
- Prialnik, D. K., Barucci, A., & Young, L. 2020, The Trans-Neptunian Solar System (1st ed.; Amsterdam: Elsevier)
- Quirico, E., Bacmann, A., Wolters, C., et al. 2023, *Icar*, **394**, 115396
- Rubino, S., Leroux, H., Lantz, C., et al. 2024, *Icar*, **415**, 116070
- Sagan, C., & Khare, B. N. 1979, *Natur*, **277**, 102
- Sakakibara, N., Yu, P. Y., Ito, T., & Terashima, K. 2020, *ApJ*, **891**, L44
- Sandford, S. A., Nuevo, M., Bera, P. P., & Lee, T. J. 2020, *ChRv*, **120**, 4616
- Schwamb, M. E., Fraser, W. C., Bannister, M. T., et al. 2019, *ApJS*, **243**, 12
- Seccull, T., Fraser, W. C., Kiersz, D. A., & Puzia, T. H. 2024, *PSJ*, **5**, 42
- Seccull, T., Fraser, W. C., & Puzia, T. H. 2021, *PSJ*, **2**, 57
- Seccull, T., Fraser, W. C., Puzia, T. H., Brown, M. E., & Schönebeck, F. 2018, *ApJ*, **855**, L26
- Sheppard, S. S. 2010, *AJ*, **139**, 1394
- Souza-Feliciano, A. C., De Prá, M., Pinilla-Alonso, N., et al. 2020, *Icar*, **338**, 113463
- Souza-Feliciano, A. C., Holler, B. J., Pinilla-Alonso, N., et al. 2024, *A&A*, **681**, L17
- Stern, S. A. 2002, *AJ*, **124**, 2297

- Strazzulla, G., Cooper, J. F., Christian, E. R., & Johnson, R. E. 2003, *CRPhy*, **4**, 791
- Tarczay, G., Forstel, M., Maksyutenko, P., & Kaiser, R. I. 2016, *InCh*, **55**, 8776
- Thirouin, A., & Sheppard, S. S. 2019, *AJ*, **158**, 53
- Turner, A. M., Abplanalp, M. J., Chen, S. Y., et al. 2015, *PCCP*, **17**, 27281
- Turner, A. M., Bergantini, A., Koutsogiannis, A. S., et al. 2021, *ApJ*, **916**, 74
- Turner, A. M., & Kaiser, R. I. 2020, *AcChR*, **53**, 2791
- Turro, N. J. 1991, Modern Molecular Photochemistry (1st ed.; Mill Valley, CA: Univ. Science Books)
- Walton, C. R., Rigley, J. K., Lipp, A., et al. 2024, *NatAs*, **8**, 556
- Wong, I., & Brown, M. E. 2016, *AJ*, **152**, 90
- Wong, I., & Brown, M. E. 2017, *AJ*, **153**, 145
- Wong, I., Mishra, A., & Brown, M. E. 2019, *AJ*, **157**, 225
- Woodward, R. B. 1941, *JACoS*, **63**, 1123
- Yeghikyan, A. 2017, *Ap*, **60**, 374
- Young, L. A., Braga-Ribas, F., & Johnson, R. E. 2020, in The Trans-Neptunian Solar System, ed. D. Prialnik et al. (1st ed.; Amsterdam: Elsevier), 127
- Zhang, C., Leyvac, V., Wang, J., et al. 2024, *PNAS*, **121**, e2320215121
- Zhang, C., Zhu, C., Turner, A. M., et al. 2023, *SciA*, **9**, eadg6936
- Zheng, W., Jewitt, D., & Kaiser, R. I. 2006a, *ApJ*, **639**, 534
- Zheng, W., Jewitt, D., & Kaiser, R. I. 2006b, *ApJ*, **648**, 753
- Zheng, W., Jewitt, D., Osamura, Y., & Kaiser, R. I. 2008, *ApJ*, **674**, 1242